A&A 581, A68 (2015)
DOI: 10.1051/0004-6361/201424155

Astronomy & Astrophysics

Stellar parameters for stars of the CoRoT exoplanet field⋆

C. Cortés[1,2,3], S. C. Maciel[2], S. Vieira[2,5], C. E. Ferreira Lopes[2,6], I. C. Leão[2], G. P. de Oliveira[2], C. Correia[2], B. L. Canto Martins[2], M. Catelan[3,4], and J. R. De Medeiros[2]

[1] Departamento de Física, Facultad de Ciencias Básicas, Universidad Metropolitana de la Educación, Av. José Pedro Alessandri 774, 7760197 Nuñoa, Santiago, Chile
e-mail: cristian.cortes@umce.cl
[2] Departamento de Física, Universidade Federal do Rio Grande do Norte, 59072-970 Natal, RN, Brazil
[3] Millennium Institute of Astrophysics (MAS), Santiago, Chile
[4] Ponticia Universidad Católica de Chile, Instituto de Astrofísica, Av. Vicuña Mackenna 4860, 782-0436 Macul, Santiago, Chile
[5] Universidade Federal de Roraima, Campus Paricarana, Av. Cap. Ene Garcez 2413, Aeroporto, 69304-000 Boa Vista, RR, Brazil
[6] Scottish Universities Physics Alliance, Wide-Field Astronomy Unit, Institute for Astronomy, School of Physics and Astronomy, University of Edinburgh, Royal Observatory, Blackford Hill, Edinburgh EH9 3HJ, UK

Received 7 May 2014 / Accepted 13 May 2015

ABSTRACT

Context. Spectroscopic observations represent a fundamental step in the physical characterization of stars and, in particular, in the precise location of stars in the HR diagram. Rotation is also a key parameter, impacting stellar properties and evolution, which modulates the interior and manifests itself on the surface of stars. To date, the lack of analysis based on large samples has prevented our understanding of the real impact of stellar parameters and rotation on the stellar evolution as well as on the behavior of surface abundances. The space missions, CoRoT and *Kepler*, are providing us with rotation periods for thousands of stars, thus enabling a robust assessment of the behavior of rotation for different populations and evolutionary stages. For these reasons, the follow-up programs are fundamental to increasing the returns of these space missions. An analysis that combines spectroscopic data and rotation/modulation periods obtained from these space missions provides the basis for establishing the evolutionary behavior of the angular momentum of solar-like stars at different evolutionary stages, and the relation of rotation with other relevant physical and chemical parameters.

Aims. To support the computation and evolutionary interpretation of periods associated with the rotational modulation, oscillations, and variability of stars located in the CoRoT fields, we are conducting a spectroscopic survey for stars located in the fields already observed by the satellite. These observations allow us to compute physical and chemical parameters for our stellar sample.

Methods. Using spectroscopic observations obtained with UVES/VLT and Hydra/Blanco, and based on standard analysis techniques, we computed physical and chemical parameters ($T_{\rm eff}$, log (g), [Fe/H], $v_{\rm mic}$, $v_{\rm rad}$, v sin (i), and A(Li)) for a large sample of CoRoT targets.

Results. We provide physical and chemical parameters for a sample comprised of 138 CoRoT targets. Our analysis shows the stars in our sample are located in different evolutionary stages, ranging from the main sequence to the red giant branch, and range in spectral type from F to K. The physical and chemical properties for the stellar sample are in agreement with typical values reported for FGK stars. However, we report three stars presenting abnormal lithium behavior in the CoRoT fields. These parameters allow us to properly characterize the intrinsic properties of the stars in these fields. Our results reveal important differences in the distributions of metallicity, $T_{\rm eff}$, and evolutionary status for stars belonging to different CoRoT fields, in agreement with results obtained independently from ground-based photometric surveys.

Conclusions. Our spectroscopic catalog, by providing much-needed spectroscopic information for a large sample of CoRoT targets, will be of key importance for the successful accomplishment of several different programs related to the CoRoT mission, thus it will help further boost the scientific return associated with this space mission.

Key words. stars: abundances – stars: rotation – stars: variables: general

1. Introduction

The Convection, Rotation, and planetary Transits (CoRoT) space mission (Baglin et al. 2007) collected a total of 161 303 point-source photometric data over a period of six years for stars exhibiting different luminosity classes and spectral types. This space mission had two main goals: 1) the detection of extra-solar planets using the transit procedure; and 2) precise stellar seismology. In addition to these two big challenges, other programs related to the CoRoT mission are helping further our understanding of a variety of important astrophysical phenomena, such as stellar activity, pulsation, and multiplicity. In this context, CoRoT provides a unique opportunity for the study of stellar rotation, which is recognized as a fundamental quantity that controls the evolution of stars, however, it is only today that the models and observations in hand to begin to address it. In this sense, CoRoT offers the necessary tools for the photometric measurements of rotation periods for a statistically robust sample of stars at different evolutionary stages and belonging to different stellar populations.

However, in spite of the large amount of high-quality photometric data obtained with CoRoT, ground-based observations

⋆ Based on observations obtained with the UVES (VLT/UT2 ESO program 077.D-0446A) and Hydra/Blanco 4m (CTIO-NOAO program P#9005) spectrographs.

are also needed to accomplish the main scientific goals of the mission. For this reason, several observational programs have increased the photometric database related to the CoRoT mission (e.g., Aigrain et al. 2009; Deleuil et al. 2009). These data enabled the establishment of the best fields and observation setups to observe with the satellite, also establishing the spectral types and luminosity classes for the stars in the CoRoT fields. Nevertheless, important uncertainties are still present in these classifications because of the variable reddening levels affecting the CoRoT fields, in addition to the still unknown chemical abundances and distances to the targets.

Spectroscopic observations are mandatory for a solid treatment of the different CoRoT scientific goals. In this sense, two large spectroscopic surveys of CoRoT targets have been carried out to date, both using multifiber observations. The first survey (Gazzano et al. 2010, G10 hereafter) combined multifiber observations with an automated procedure for the determinations of different stellar parameters, whereas the second was dedicated essentially to spectral classification (Sebastian et al. 2012).

In the context of the physical characterization of CoRoT targets, we carried out a large spectroscopic survey focused on the brightest F-, G-, and K-type stars in the CoRoT exoplanet fields LRc01 and LRa01, using the multifiber spectrographs UVES/VLT and Hydra/Blanco, with high and medium spectral resolution, respectively. Using these observations, we applied a homogeneous procedure for the determination of different stellar parameters, including effective temperature ($T_{\rm eff}$), surface gravity ($\log(g)$), overall metallicity ([Fe/H]), radial velocity ($v_{\rm rad}$), projected rotational velocity ($v \sin(i)$), and microturbulence ($v_{\rm mic}$). The main goal of this paper is to present the corresponding catalog. We also present the mean values for stellar parameters of the two stellar populations in the CoRoT anticenter/center direction. The paper is structured as follows: in Sect. 2 we describe the observations and data reduction. Section 3 describes how we derived the stellar parameters for the stars in our sample, and Sect. 4 contains our main results. Finally, we draw our conclusions in Sect. 5.

2. Observations

The present stellar sample is composed of 138 stars of spectral types F, G, and K, with visual magnitudes V between 10 to 14, located in two exoplanet fields observed by CoRoT, namely the Galactic center (LRc01: Long Run Center 01) and the Galactic anticenter (LRa01: Long Run Anticenter 01) fields. We selected the sample using as criteria the visual magnitude V, the spectral type, and the luminosity classes defined by Deleuil et al. (2009) for CoRoT targets. We selected stars belonging to luminosity classes II, III, IV, and V considering the range in V and spectral type defined above. Our sample is comprised of the brightest stars in both CoRoT fields, and is thus not fully representative of the magnitude and color distribution of CoRoT stars.

To obtain a physical characterization for these stars, a series of spectroscopic observations were carried out using two spectrographs. A sample of 53 stars was observed using the high-resolution UVES spectrograph (hereafter UVES stars) mounted on the Kuyen/VLT 8.2 m telescope, located in Cerro Paranal, Chile, in the course of different observing runs in 2006. The UVES standard setup DICH-2 (390–760 nm) with a 0.9 arcsec slit was used, allowing us to obtain high-resolution ($R \approx 47\,000$) and high signal-to-noise ($S/N > 100$) spectra. The main characteristics of the targets and the observation dates are given in Table 1.

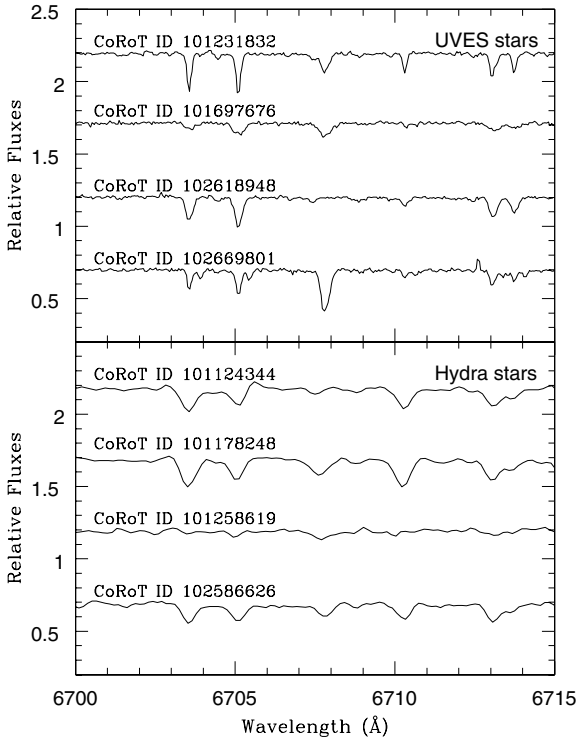

Fig. 1. Some spectra of the stars contained in the sample. Spectra collected using the UVES spectrograph are show in the *upper panel*, whereas the *lower panel* shows spectra collected using the Hydra spectrograph.

A complementary sample of 85 stars was observed using the Hydra multifiber echelle spectrograph (henceforth Hydra stars), mounted on the Blanco 4m telescope at the Cerro Tololo Interamerican Observatory, located in Cerro Tololo, Chile. The filters $E5187$ (509–525 nm) and $E6757$ (656–681 nm) with a 200 micron slit were used, allowing us to collect spectra with medium resolution ($R \approx 17\,000$ and 15 000, respectively) and signal-to-noise ratio $70 < S/N < 200$. The $E5187$ filter was chosen because it covers a spectral region with five Fe II lines, whereas the $E6757$ was chosen because several Fe I lines and a Li doublet (at ≈671 nm) are located in spectral window. Also, a few stars, with accurate previous measurements of $v \sin(i)$ and with FGK spectral types, were also observed with the same Hydra setups (Melo et al. 2001) to construct a calibration for the determination of $v \sin(i)$ for the Hydra stars in our sample. Figure 1 shows examples of these observations using both instruments.

Table 2 shows the setup used in Hydra observations. For the targets, we also compiled luminosity classes, V-band magnitudes, and color indices from the CoRoT database[1], as well as JHKs magnitudes from the Two-Micron All-Sky Survey (2MASS) database (Skrutskie et al. 1996). The main characteristics of the targets and the observation dates, and corresponding luminosity classes (from the CoRoT and 2MASS databases) are given in Tables 3 and 4.

The reduction of UVES stars data was done using the standard UVES data reduction pipeline (Ballester et al. 2000). Hydra data were reduced using the *dohydra* task in IRAF[2]. Both

[1] Available in http://idoc-corot.ias.u-psud.fr/index.jsp

[2] IRAF is distributed by the National Optical Astronomy Observatories, which are operated by the Association of Universities for Research in Astronomy, Inc., under cooperative agreement with the National Science Foundation.

Table 1. CoRoT IDs, ephemerides, details of observations, photometry, and estimated luminosity classes (LC) for the UVES stars.

CoRoT ID	RA (J2000)	Dec (J2000)	Heliocentric Julian Date (HJD)	T_{exp} (s)	S/N	V (mag)	$(B-V)$ (mag)	J (mag)	H (mag)	K (mag)	LC	Field
100532655	19:23:03.118	+01:34:55.60	2006 Apr. 23	1000	128	12.03	0.93	10.38	10.01	9.93	IV	LRc01
100537408	19:23:04.841	+01:46:24.49	2006 May 16	1000	130	12.23	0.85	10.60	10.36	10.22	III	LRc01
100931549	19:25:21.353	+00:11:07.94	2006 May 23	1000	129	12.48	0.89	10.93	10.58	10.48	IV	LRc01
100932329	19:25:21.593	+00:11:31.02	2006 May 23	1000	200	12.12	1.01	10.33	9.88	9.76	IV	LRc01
101041358	19:26:00.737	+00:36:33.01	2006 Jun. 17	1000	131	12.43	0.90	10.71	10.27	10.18	V	LRc01
101043867	19:26:01.891	−00:02:49.67	2006 Jun. 17	1000	111	12.42	0.85	10.83	10.49	10.43	IV	LRc01
101056542	19:26:07.651	+00:11:03.37	2006 Jun. 17	1000	122	12.43	0.67	11.14	10.90	10.85	IV	LRc01
101076647	19:26:17.654	+00:12:09.00	2006 Apr. 19	1000	102	12.43	0.90	10.73	10.40	10.32	IV	LRc01
101102758	19:26:27.502	+00:32:20.15	2006 Apr. 23	1000	124	12.43	1.00	10.62	10.24	10.10	IV	LRc01
101128747	19:26:37.291	+00:02:58.96	2006 Jun. 17	1000	141	12.00	0.87	10.46	10.22	10.11	III	LRc01
101204408	19:27:05.707	+00:32:05.06	2006 Jun. 17	1000	142	13.58	1.52	10.74	10.00	9.86	V	LRc01
101208246	19:27:07.138	+00:27:19.33	2006 Jun. 17	1000	109	12.43	1.02	10.61	10.20	10.08	IV	LRc01
101231832	19:27:16.032	+00:17:35.59	2006 Jun. 17	1000	150	12.13	0.90	10.47	10.08	10.02	IV	LRc01
101462309	19:28:53.256	−00:04:41.20	2006 Jun. 18	1000	130	12.13	0.89	10.55	10.22	10.15	V	LRc01
101476063	19:28:58.836	+00:40:16.72	2006 Jun. 18	1000	105	12.20	0.97	10.46	10.07	9.93	III	LRc01
101478005	19:28:59.618	−00:07:21.76	2006 Jun. 18	1000	120	12.24	0.99	10.52	10.07	9.99	IV	LRc01
101565378	19:29:35.662	−00:12:26.06	2006 May 30	1000	174	12.33	0.80	10.87	10.56	10.47	IV	LRc01
101613938	19:29:56.532	+00:01:31.04	2006 May 30	1000	167	12.23	0.86	10.70	10.40	10.35	V	LRc01
101697676	19:30:35.563	+00:03:20.05	2006 May 30	1000	153	12.37	0.80	10.99	10.67	10.60	V	LRc01
102585563	06:41:02.086	−00:33:16.38	2006 Sept. 07	1000	166	16.12	1.08	13.71	13.09	12.99	V	LRa01
102585613	06:41:02.184	+00:19:38.39	2006 Sept. 06	1000	188	12.34	0.44	11.31	11.11	11.03	III	LRa01
102589564	06:41:08.995	+00:48:20.41	2006 Sept. 07	1000	133	12.46	0.50	11.49	11.29	11.21	V	LRa01
102591896	06:41:12.994	−00:45:13.54	2006 Sept. 03	1000	150	12.25	0.54	11.28	11.09	11.00	V	LRa01
102603174	06:41:31.006	−00:57:44.14	2006 Sept. 10	1000	138	12.08	0.56	11.14	10.86	10.81	V	LRa01
102604055	06:41:32.222	+00:59:10.75	2006 Sept. 10	1000	126	12.35	0.46	11.41	11.21	11.15	V	LRa01
102605405	06:41:34.037	+00:00:30.24	2006 Sept. 13	1000	211	12.08	0.60	10.97	10.69	10.63	V	LRa01
102606185	06:41:35.021	+00:54:44.68	2006 Sept. 13	1000	105	13.44	0.56	12.39	12.11	12.10	V	LRa01
102611980	06:41:42.962	−00:24:33.84	2006 Sept. 13	1000	117	12.41	0.65	11.30	11.00	10.97	V	LRa01
102614844	06:41:46.882	+00:21:40.72	2006 Sept. 22	1000	91	12.50	0.83	11.13	10.78	10.72	IV	LRa01
102616719	06:41:49.716	−01:32:02.26	2006 Aug. 31	1000	123	12.31	0.59	11.30	11.08	10.99	V	LRa01
102618948	06:41:52.913	+00:24:13.86	2006 Sept. 22	1000	134	12.01	0.66	10.88	10.63	10.55	III	LRa01
102620828	06:41:55.704	−00:59:37.90	2006 Sept. 24	1000	120	12.36	0.85	10.90	10.47	10.37	III	LRa01
102654716	06:42:42.254	+00:47:29.00	2006 Sept. 23	1000	171	12.15	0.55	11.06	10.83	10.74	III	LRa01
102657182	06:42:45.377	−00:32:21.05	2006 Sept. 24	1000	116	12.35	0.78	10.98	10.60	10.55	III	LRa01
102658181	06:42:46.610	+00:53:40.09	2006 Sept. 24	1000	103	12.38	0.71	11.12	10.80	10.73	V	LRa01
102659670	06:42:48.432	+00:29:03.59	2006 Sept. 25	1000	129	12.01	0.51	11.07	10.85	10.81	III	LRa01
102663892	06:42:53.772	−01:17:53.56	2006 Sept. 27	1000	145	12.36	0.60	11.31	11.03	10.98	V	LRa01
102669038	06:43:00.288	+00:49:01.52	2006 Sept. 26	750	112	12.38	0.46	11.37	11.17	11.09	III	LRa01
102669801	06:43:01.198	+00:14:26.81	2006 Sept. 25	1000	111	12.34	0.66	11.10	10.80	10.73	III	LRa01
102676872	06:43:09.950	−01:27:26.03	2006 Sept. 25	1000	120	12.19	0.98	10.28	9.81	9.68	III	LRa01
102678564	06:43:12.110	−00:26:59.78	2006 Sept. 25	1000	130	12.11	0.51	11.13	10.93	10.86	V	LRa01
102679796	06:43:13.630	+00:45:08.89	2006 Sept. 25	1000	127	12.04	0.50	11.06	10.83	10.79	IV	LRa01
102686019	06:43:21.432	−00:04:27.05	2006 Sept. 25	1000	130	12.20	0.50	11.30	11.07	11.02	V	LRa01
102687759	06:43:23.638	+00:12:21.89	2006 Sept. 26	1000	140	12.21	0.56	11.14	10.86	10.85	V	LRa01
102692093	06:43:29.011	+01:02:31.52	2006 Oct. 01	1000	132	12.47	0.61	11.25	10.94	10.87	III	LRa01
102705308	06:43:44.971	+00:55:50.41	2006 Sept. 27	1000	167	12.39	0.96	10.59	10.09	10.00	III	LRa01
102709247	06:43:50.210	−01:11:03.01	2006 Sept. 27	1000	142	12.46	0.77	11.25	10.91	10.88	III	LRa01
102718064	06:44:02.532	+00:27:04.14	2006 Sept. 27	1000	167	15.91	0.73	14.41	14.26	13.91	V	LRa01
102738854	06:44:31.608	−00:18:21.10	2006 Sept. 27	1000	126	12.25	0.63	11.12	10.85	10.80	IV	LRa01
102740520	06:44:33.814	−00:50:35.77	2006 Sept. 05	1000	103	12.40	0.79	11.19	10.88	10.82	V	IRa01
102741215	06:44:34.738	−01:55:45.69	2006 Sept. 05	1000	126	12.41	0.63	11.25	10.97	10.91	V	LRa01
102764866	06:45:06.610	−01:05:31.81	2006 Sept. 28	1000	150	12.14	0.63	11.01	10.71	10.63	IV	LRa01
102772347	06:45:16.702	−00:56:54.06	2006 Sept. 28	1000	142	12.14	0.66	10.97	10.65	10.59	IV	LRa01

Table 2. Setup used for Hydra observations.

Field	Number of exposures	T_{exp} (s)	Heliocentric Julian Date (HDJ)	Filter
LRa01	2	2700	2009 Oct. 04	*E*5187
LRc01	2	2700	2009 Oct. 04	*E*5187
LRa01	2	2200	2009 Oct. 04	*E*6757
LRc01	2	2850	2009 Oct. 04	*E*6757

reductions follow the usual reduction steps (bias, flat-field, and background corrections, fiber order definition, wavelength calibration of the spectra with Th-Ar lamp spectra, and extraction of the spectra). Then we use IRAF to normalize the spectra to a pseudocontinuum level and to bring the reduced spectra to the rest frame. Cosmic rays were extracted using the procedures described in van Dokkum (2001).

3. Stellar properties

3.1. Radial velocities v_{rad}

We obtained radial velocities v_{rad} with the *fxcor* task (Tonry & Davis 1979) in IRAF. Because the stars of the UVES sample present T_{eff} close to the solar value, we cross-correlated the UVES spectra with a spectrum of the Sun (Hinkle et al. 2000). We then converted the shifts into radial velocities of the stars, and we applied a barycentric correction. On the other hand, because the Hydra stars present a greater spread in temperatures and luminosity classes, the spectra were cross-correlated with synthetic spectra of the Sun and an RGB star (T_{eff} = 4000 K, log (g) = 1.0 dex and [Fe/H] = 0.0 dex) to compare differences in the determinations of radial velocities. We computed the spectra with the Turbospectrum code (Alvarez & Plez 1998) and MARCS atmosphere models with solar abundances (Gustafsson et al. 2008). In Fig. 2 small differences can be found between the radial velocities derived using the synthetic spectra (averaging about -0.27 ± 0.37 km s^{-1}). We opted to use the values found using the synthetic solar spectrum, and applied a barycentric correction. The typical errors in radial velocities for Hydra stars are lower than 0.5 km s^{-1}. On the other hand, we also computed a synthetic solar spectrum for the UVES spectral resolution, which we used to obtain v_{rad} for the UVES sample, to find systematic errors in the Hydra v_{rad} measured using synthetic spectra. We found that our measurements of v_{rad} using synthetic spectra present a systematic difference of about -0.75 ± 1.66 km s^{-1} with those derived with observed solar spectrum, and is thus not significant.

3.2. Rotation velocities $v \sin(i)$

The $v \sin(i)$ measurements of our targets were computed using two procedures. For the case of UVES stars, the $v \sin(i)$ values were determined using the same procedure as in Canto Martins et al. (2011). Following these authors, the resulting spectra (taking into account the instrumental profile of UVES) are convolved with rotational profiles to adjust the broadening observed in the iron lines (profile fitting) located between 6700 and 6715 Å.

The $v \sin(i)$ values for the Hydra stars were computed (using the *fxcor* task) with a cross-correlation function (CCF) especially calibrated for the Hydra spectrograph. We then followed the same procedure decribed before for the UVES stars. As is described in Recio-Blanco et al. (2002) and

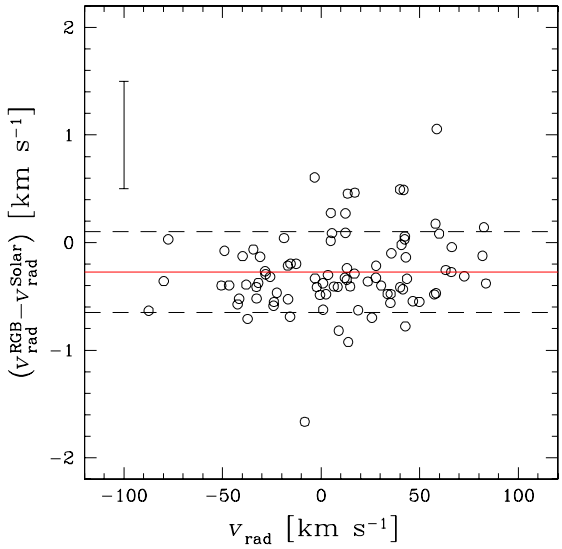

Fig. 2. Comparison between the v_{rad} measurements for the Hydra sample obtained using different synthetic spectra. The $v_{rad}^{RGB} - v_{rad}^{Solar}$ represents the difference between the v_{rad} obtained when the Hydra spectra are cross-correlated with synthetic spectra for a RGB star and the Sun, respectively. The red line represents the mean value of $v_{rad}^{RGB} - v_{rad}^{Solar}$ and the standard deviation is presented using black dashed lines. Also, the typical error in v_{rad} measurements for Hydra stars is shown using an error bar.

Lucatello & Gratton (2003), the relation between $v \sin(i)$ and the corrected width σ_{obs0} of the CCF is

$$v \sin(i) = A \sqrt{(\sigma_{obs0})^2 - (\sigma_0)^2} \text{ km s}^{-1}, \quad (1)$$

where A and σ_0 are the so-called coupling constant and the non-rotational contribution to the CCF width, respectively. As mentioned in Melo et al. (2001), σ_0 depends on different broadening mechanisms (magnetic field, instrumental profile, thermal broadening, etc.), which is related to object star and the template used, but does not depend on rotation.

Since the setup *E*5187 presents the highest resolution in our Hydra observations, it was chosen to determine the $v \sin(i)$ values. We used FGK stars with reliable $v \sin(i)$ determinations as templates and calibrators, which were observed during our observing runs. The $v \sin(i)$ values and photometry for these stars are compiled in Table 4.

The *fxcor* task allowed us to obtain the uncorrected width of the CCF (σ_{obs}), which has a contribution from the template used (σ_t) in deriving the CCF. The σ_t can be determined with an autocorrelation for each template, as is described in Eq. (4) of Lucatello & Gratton (2003). For each star used as template we obtained several spectra, which allowed us to avoid the autocorrelation of the same spectrum. The σ_{obs} and σ_t are related with the corrected width σ_{obs0} through the following equation:

$$(\sigma_{obs0})^2 = (\sigma_{obs})^2 - (\sigma_t)^2. \quad (2)$$

The mean values of σ_{obs} and σ_t for each template are listed in Table 5, whereas the mean values of σ_{obs} for each calibrator star are listed in Table 6. Finally, using a linear fit in the plane $[(\sigma_{obs0})^2, (v \sin(i))^2]$ the following relation between $v \sin(i)$ and σ_{obs0} was obtained:

$$v \sin(i) = (0.861 \pm 0.017) \sqrt{\sigma_{obs0}^2 - (21.404 \pm 0.835)^2} \text{ km s}^{-1}.$$

The errors in these coefficients are associated with the errors in the slopes of the linear fit. In Fig. 3 we show the final calibration,

Table 3. Main characteristics for the Hydra stars.

CoRoT ID	RA (J2000)	Dec (J2000)	S/N	V (mag)	$(B-V)$ (mag)	J (mag)	H (mag)	K (mag)	LC	Field
101057962	19:26:08.33	−00:25:22.80	167	12.69	1.44	9.95	9.22	9.07	V	LRc01
101066444	19:26:12.18	+00:01:28.60	123	13.37	1.81	10.04	9.25	9.03	II	LRc01
101124344	19:26:35.61	−00:27:25.00	187	13.18	1.24	10.92	10.39	10.26	III	LRc01
101154362	19:26:46.93	−00:12:23.80	170	13.13	1.34	10.77	10.13	9.98	V	LRc01
101165983	19:26:51.33	−00:11:36.20	85	13.55	1.40	10.98	10.28	10.12	V	LRc01
101178248	19:26:55.94	+00:06:04.30	168	12.38	1.48	9.71	9.04	8.83	V	LRc01
101237841	19:27:18.30	−00:18:36.60	158	12.71	1.47	9.99	9.24	9.04	V	LRc01
101249643	19:27:22.85	−00:11:34.00	141	13.15	0.75	11.71	11.37	11.32	IV	LRc01
101258619	19:27:26.19	−00:00:00.90	132	12.76	1.28	10.46	9.84	9.73	V	LRc01
101268962	19:27:30.19	+00:05:46.20	91	13.45	1.28	11.05	10.43	10.32	V	LRc01
101305750	19:27:43.47	−00:23:44.20	120	13.25	1.25	11.02	10.46	10.36	IV	LRc01
101319580	19:27:49.44	−00:13:25.20	118	12.64	1.42	10.15	9.58	9.41	V	LRc01
101346995	19:28:02.83	+00:20:23.39	105	13.19	1.68	10.11	9.37	9.13	II	LRc01
101347642	19:28:03.14	−00:21:33.90	93	12.72	1.44	10.15	9.54	9.37	V	LRc01
101347760	19:28:03.20	+00:16:07.32	123	13.03	1.20	10.63	10.09	9.92	V	LRc01
101358013	19:28:08.16	−00:20:27.30	128	12.65	0.85	10.93	10.56	10.47	IV	LRc01
101392071	19:28:24.37	+00:04:02.39	99	12.96	1.70	9.89	9.14	8.87	III	LRc01
101411168	19:28:32.30	+00:08:48.98	176	12.45	1.44	9.87	9.23	9.05	V	LRc01
101421386	19:28:36.46	+00:13:53.22	78	13.08	1.27	10.66	10.05	9.90	V	LRc01
101422730	19:28:37.00	+00:35:47.90	116	13.44	1.41	10.91	10.28	10.08	III	LRc01
101423629	19:28:37.35	+00:08:34.15	92	13.39	1.49	10.73	10.07	9.88	V	LRc01
101433432	19:28:41.46	+00:02:59.42	144	13.52	1.47	10.88	10.25	10.07	V	LRc01
101451115	19:28:48.69	+00:05:19.28	151	13.39	1.38	10.79	10.10	9.93	V	LRc01
101455904	19:28:50.63	+00:01:43.21	132	12.95	0.94	11.34	10.92	10.83	V	LRc01
101458937	19:28:51.90	+00:10:25.10	144	13.22	1.52	10.39	9.70	9.48	V	LRc01
101461526	19:28:52.93	+00:03:52.74	145	13.44	1.63	10.43	9.65	9.42	II	LRc01
101464585	19:28:54.20	+00:27:25.52	114	13.49	1.70	10.39	9.61	9.35	II	LRc01
101479386	19:29:00.19	+00:27:51.30	156	13.01	1.51	10.26	9.60	9.42	V	LRc01
101483826	19:29:02.05	+00:25:04.22	123	12.71	1.44	10.08	9.46	9.30	V	LRc01
101489251	19:29:04.27	+00:35:50.71	134	13.10	1.79	9.81	8.98	8.72	II	LRc01
101489977	19:29:04.55	+00:25:45.62	127	13.04	1.51	10.45	9.81	9.63	I	LRc01
101492953	19:29:05.79	+00:09:00.32	158	12.68	1.29	10.38	9.78	9.59	V	LRc01
101519854	19:29:16.94	+00:03:50.33	140	13.27	1.08	11.34	10.92	10.86	IV	LRc01
101536086	19:29:23.83	+00:37:03.72	120	13.14	1.38	10.64	9.97	9.87	V	LRc01
101538522	19:29:24.87	−00:00:17.75	157	13.02	1.63	9.94	9.16	8.94	III	LRc01
101549180	19:29:29.41	+00:00:11.41	169	12.13	0.82	10.59	10.28	10.18	V	LRc01
101550759	19:29:30.06	+00:04:39.07	117	13.13	1.45	10.54	9.88	9.70	V	LRc01
101552742	19:29:30.81	+00:15:15.48	137	13.43	1.32	10.87	10.28	10.11	V	LRc01
101555541	19:29:31.89	+00:23:40.09	123	12.63	1.38	10.08	9.41	9.27	V	LRc01
101561050	19:29:34.00	+00:15:32.94	105	12.47	1.47	9.78	9.11	8.92	V	LRc01
101562508	19:29:34.56	+00:08:29.36	130	13.14	1.39	10.61	9.97	9.79	V	LRc01
101565091	19:29:35.55	+00:36:32.08	224	12.60	0.98	10.75	10.41	10.30	I	LRc01
101569925	19:29:37.39	+00:30:53.71	111	13.16	1.45	10.54	9.92	9.74	V	LRc01
101598546	19:29:49.09	+00:25:32.38	125	13.53	1.51	10.83	10.20	10.06	V	LRc01
101599646	19:29:49.59	+00:18:20.16	95	12.93	0.86	11.26	10.95	10.85	V	LRc01
101600807	19:29:50.14	+00:27:10.40	98	12.99	1.55	10.18	9.51	9.35	V	LRc01
101612300	19:29:55.73	+00:15:20.70	131	12.67	1.08	10.59	10.16	10.06	IV	LRc01
101622447	19:30:00.67	+00:27:25.34	102	13.51	1.50	10.76	10.12	9.95	V	LRc01
101626971	19:30:02.86	+00:06:48.31	154	13.30	1.32	10.74	10.17	10.00	V	LRc01
101627005	19:30:02.88	+00:24:24.41	110	12.93	0.98	11.09	10.77	10.67	IV	LRc01
101635594	19:30:07.24	+00:25:09.41	78	13.49	1.74	10.36	9.66	9.46	III	LRc01
101642292	19:30:10.61	+00:03:55.08	132	12.61	1.47	10.00	9.35	9.17	V	LRc01
101665008	19:30:21.98	+00:18:46.55	111	13.56	1.45	10.83	10.19	9.99	V	LRc01
102574603	06:40:43.20	+00:51:16.10	87	12.37	0.58	11.26	11.00	10.92	III	LRa01
102580280	06:40:52.98	+00:39:57.30	150	13.20	0.73	11.70	11.33	11.23	III	LRa01
102586626	06:41:03.94	+00:59:26.00	177	12.30	1.25	9.87	9.24	9.09	III	LRa01
102598042	06:41:23.33	+00:53:08.70	60	13.30	0.79	11.92	11.54	11.48	IV	LRa01
102602960	06:41:30.72	+00:40:55.50	97	13.10	0.63	11.86	11.59	11.48	V	LRa01
102612876	06:41:44.23	+00:27:46.00	124	13.08	1.29	10.44	9.77	9.61	III	LRa01
102615343	06:41:47.66	+00:45:43.50	62	13.02	0.54	11.97	11.71	11.69	V	LRa01
102625766	06:42:03.03	+00:39:04.40	77	12.69	0.57	11.61	11.33	11.27	III	LRa01
102627939	06:42:06.25	+00:29:57.90	150	13.15	0.77	11.77	11.46	11.37	III	LRa01
102637778	06:42:20.33	+00:31:50.70	96	13.24	0.67	12.00	11.68	11.60	III	LRa01
102662415	06:42:51.90	+00:33:40.30	120	12.98	1.08	11.03	10.52	10.38	III	LRa01
102694697	06:43:32.20	−00:32:21.95	133	12.36	1.25	10.10	9.49	9.35	III	LRa01

Table 3. continued.

CoRoT ID	RA (J2000)	Dec (J2000)	S/N	V (mag)	$(B-V)$ (mag)	J (mag)	H (mag)	K (mag)	LC	Field
102694848	06:43:32.40	−00:38:31.13	96	12.61	1.38	10.15	9.52	9.32	III	LRa01
102695542	06:43:33.28	−00:39:35.24	170	12.62	1.09	10.46	10.01	9.85	III	LRa01
102697221	06:43:35.29	−00:43:32.74	200	12.12	1.23	9.93	9.30	9.16	III	LRa01
102705009	06:43:44.57	−00:29:03.05	138	12.19	0.67	11.05	10.74	10.69	V	LRa01
102705076	06:43:44.66	−00:44:53.84	60	13.28	0.75	11.89	11.48	11.39	III	LRa01
102706020	06:43:45.85	−00:36:23.76	94	12.67	1.12	10.52	9.95	9.81	III	LRa01
102728377	06:44:17.43	−00:29:26.84	103	11.83	0.58	10.77	10.48	10.41	V	LRa01
102730409	06:44:20.10	−00:43:49.40	76	13.14	0.63	11.98	11.69	11.63	III	LRa01
102735621	06:44:27.19	−00:27:49.75	84	12.86	0.64	11.69	11.42	11.35	III	LRa01
102740367	06:44:33.64	−00:44:07.62	120	13.24	0.70	11.98	11.66	11.59	V	LRa01
102743491	06:44:37.76	−00:23:37.21	90	13.10	0.82	11.64	11.29	11.20	III	LRa01
102743929	06:44:38.32	−00:33:34.34	122	12.60	1.14	10.53	9.96	9.80	III	LRa01
102754990	06:44:53.16	−00:38:04.13	114	12.26	1.18	10.03	9.45	9.33	III	LRa01
102758371	06:44:57.73	−00:31:03.76	134	11.62	0.56	10.61	10.34	10.31	III	LRa01
102767494	06:45:10.17	−00:38:53.74	95	12.98	0.74	11.64	11.27	11.24	V	LRa01
102768747	06:45:11.82	−00:24:49.86	97	11.74	0.63	10.61	10.30	10.22	V	LRa01
102769088	06:45:12.28	−00:49:14.09	105	12.00	1.22	9.80	9.25	9.10	III	LRa01
102789493	06:45:39.68	−00:31:59.77	62	13.47	1.12	11.34	10.84	10.66	III	LRa01
102789962	06:45:40.31	−00:38:06.36	99	12.40	0.51	11.47	11.27	11.22	III	LRa01
102792032	06:45:43.18	−00:35:51.14	108	12.25	1.23	9.90	9.28	9.13	III	LRa01

Table 4. Main characteristics and rotation velocities $v \sin(i)$ of calibrator stars.

ID	# spectra	T_{exp} (s)	Date	Hydra filter	V (mag)	$(B-V)$ (mag)	$v \sin(i)$ (km s^{-1})	References
HD 96843	2	600	2009 Oct. 04	*E*5187	8.36	0.66	13.0	1
HD 101117	2	600	2009 Oct. 04	*E*5187	7.87	0.59	9.0	2
HD 113226	8	7	2009 Oct. 04	*E*5187	2.83	0.93	3.0	3
HD 113553	3	600	2009 Oct. 04	*E*5187	8.33	0.68	12.0	1
HD 141710	2	600	2009 Oct. 04	*E*5187	8.93	0.14	30.0	1
HD 150108	2	600	2009 Oct. 04	*E*5187	8.23	0.84	21.0	1
HD 165760	3	30	2009 Oct. 04	*E*5187	4.67	0.95	2.6	3

References. (1) Cutispoto et al. (2002); (2) Nordström et al. (2004); (3) Melo et al. (2001).

Table 5. Observed broadening σ_{obs} and σ_t for template stars.

ID	# spectra	$\langle\sigma^P_{obs}\rangle$ km s^{-1}	$\Delta\sigma_{obs}$ km s^{-1}	$\langle\sigma_t\rangle$ km s^{-1}
HD 113226	8	29.9	0.6	21.2
HD 165760	3	30.5	0.1	21.5

which presents a good agreement with the reference values of $v \sin(i)$ for calibrator stars.

These $v \sin(i)$ values were used as reference to obtain new measurements of $v \sin(i)$ values using the setup *E*6757 and the same method described for UVES stars. Note that the setup *E*6757 contains the spectral region between 6700 and 6715 Å. Small differences were found between $v \sin(i)$ values derived using both methods. Since we use the profile fitting to derive lithium abundances (as is described in Sect. 4.4), the final values of $v \sin(i)$ for the Hydra stars are those derived from the profile fitting.

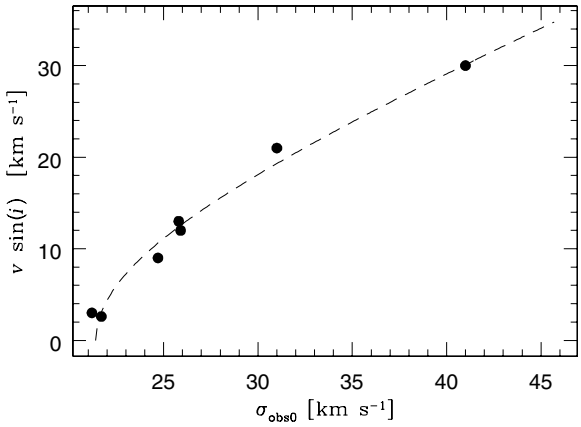

Fig. 3. CCF-$v \sin(i)$ calibration for the Hydra spectrograph. The dashed line represents the function found and black points represent the values for the calibrator stars, respectively.

3.3. Effective temperatures T_{eff}, surface gravities log (*g*), iron abundance [Fe/H], and microturbulence velocity v_{mic}

Because our stellar sample is comprised of stars belonging to the field, it is important to have an estimation of their stellar parameters, which were used to avoid mistakes in the determination of the final parameters. In this sense, as a first step in the derivation of atmospheric parameters, we used the 2MASS *JHK* near-infrared photometry and the CoRoT database mean values of $\langle V \rangle$ and $\langle (B-V) \rangle$ to obtain a first estimation of the effective temperature for our sample. Specifically, we used the

Table 6. Observed broadening σ_{obs} and σ_{obs0} for calibrator stars.

	Template						
	HD 113226[a]		HD 165760[b]				
Calibrator	$\langle\sigma_{obs}\rangle$ km s^{-1}	$\Delta\sigma_{obs}$ km s^{-1}	$\langle\sigma_{obs}\rangle$ km s^{-1}	$\Delta\sigma_{obs}$ km s^{-1}	$\langle\sigma_{obs0}\rangle^a$ km s^{-1}	$\langle\sigma_{obs0}\rangle^b$ km s^{-1}	$\langle\sigma_{obs0}\rangle$ km s^{-1}
HD 96843	33.4	0.3	33.5	0.1	25.8	25.7	25.8
HD 101117	32.6	0.4	32.8	0.1	24.7	24.7	24.7
HD 113226	...	...	30.2	0.5	...	21.2	21.2
HD 113553	33.5	0.4	33.7	0.1	25.9	25.9	25.9
HD 141710	46.2	0.3	46.2	0.2	41.1	40.9	41.0
HD 150108	37.5	0.4	37.7	0.3	31.0	30.9	31.0
HD 165760	30.3	0.5	...	...	21.7	...	21.7

mean CoRoT color index $(B-V)$ and the calibrations of Flower (1996) corrected by Torres (2010) to calculate the photometric effective temperature $T_{\rm eff}(B-V)$. In the same way, we calculated the photometric effective temperature $T_{\rm eff}(J-K)$ using the 2MASS color index $(J-K)$, the CoRoT luminosity classes, and the calibrations of Alonso et al. (1996, 1999). We derived these temperatures without reddening corrections (see Sect. 4.3 for detailed discussion). Also, we found errors at levels of 0.04 mag in the $(J-K)$ for the stars in our sample, which implies errors at levels of 130 K in $T_{\rm eff}(J-K)$. No errors are informed in the CoRoT database for $(B-V)$.

We used the average between both photometric temperatures as our initial estimation for the spectroscopic temperature. At the same time, we estimated the initial values of surface gravities $\log(g)$ using the CoRoT luminosity classes and interpolations in tables of infrared synthetic colors computed with ATLAS9 by R. Kurucz[3]. These initial estimation can present important errors, produced by reddening and bad identification of CoRoT luminosity classes (see Fig. 8 in G10). In fact we found differences of about >500 K between photometric and spectroscopic temperatures, which implies high rates of extinction in the CoRoT fields (see Sect. 4.3). For this reason we stress that these initial values were used only as a starting point to obtain the final parameters and, in any case, they constrained the searching of spectroscopic temperatures.

We determined final values of the atmospheric parameters and their respective errors using the Turbospectrum code and MARCS atmosphere models with solar abundances. Solar abundances were taken from Asplund et al. (2005), and the collisional damping treatment was performed based on the work of Barklem and co-workers (Barklem et al. 2000a,b; Barklem & Piskunov 2003; Barklem & Aspelund-Johansson 2005). To compute synthetic spectra with the Turbospectrum code, we took atomic (see below) and molecular line lists into account, including TiO (Plez 1998), VO (Alvarez & Plez 1998), and CN and CH (Hill et al. 2002). The Turbospectrum code uses equivalent widths (EW) to compute abundances A(Fe) corresponding to the different Fe lines[4]. The list of Fe lines used was compiled and corrected by Canto Martins et al. (2011, see their Table 6). This list is composed of 91 and 14 lines of Fe I and II, respectively. There are differences in the number of iron lines used to characterize the stars because our sample was observed using two instruments and different setups. In particular, for UVES stars, we used all lines compiled by Canto Martins et al. (2011), whereas for the Hydra stars 33 of the lines (28 Fe I lines and 5 Fe II lines) in the intervals 5090−5250 Å and 6560−6810 Å were used. We measured EW values with the DAOSPEC code (Stetson & Pancino 2008). Using excitation equilibrium for the Fe I abundances, Fe I/Fe II ionization equilibrium, and the equilibrium of the A(Fe) values and their respective EW values, we can derive effective temperatures $T_{\rm eff}$, surface gravities $\log(g)$, and microturbulence velocities $v_{\rm mic}$, respectively. Starting from the photometric parameters, we ran the Turbospectrum code iteratively using MARCS atmosphere models with different parameters to find the three equilibria, thus defining the final parameters. Figure 4 presents an example of physical and chemical parameter determinations using the equilibria (slopes equal to zero in the planes shown in this figure) for both a UVES star and a Hydra star.

The errors in $T_{\rm eff}$ and $v_{\rm mic}$ are obtained from the errors in the slopes that define the equilibria described above. We change one of these parameters, keeping the others fixed, and compute a new atmospheric model. We found the error when the slope of the new fit became equal to its respective slope error. The error in [Fe/H] is equal to slope error in excitation equilibrium for the Fe I abundance. Finally, the error in $\log(g)$ is found when the difference between A(FeI) and A(FeII) is equal to the square root of the sum of the squares of the errors in A(FeI) and A(FeII).

3.4. The Li abundance determinations

The Li abundances A(Li)[5] for *UVES* and Hydra stars were calculated by fitting the observed profile with a synthetic profile of the Li doublet located at ~6708 Å. The synthetic spectrum was computed using the Turbospectrum code. Figure 5 shows four examples showing the method used to determine the A(Li).

The error $\sigma_{A(\rm Li)}$ in this abundance is related to the errors in the physical and chemical parameters; more specifically, the magnitude of this error is directly related to the error in $T_{\rm eff}$, and the errors in the other stellar parameters, such as $\log(g)$, $v_{\rm mic}$, and $v\sin(i)$, produce minor effects in the measurements of A(Li). We determined new lithium abundances using synthetic spectra reflecting the errors in the four stellar parameters described above, which we called $A(\rm Li)^j_{\rm ER}$. Then, the final error $\sigma_{A(\rm Li)}$ is equal to the square root of the sum of the squares of the difference between A(Li) and $A(\rm Li)^j_{\rm ER}$, as is described in the following equation:

$$\sigma_{A(\rm Li)} = \sqrt{\sum_{j=1}^{j=4}\left(A(\rm Li) - A(\rm Li)^j_{ER}\right)^2}. \quad (3)$$

[3] These tables are available on the Kurucz webpage http://kurucz.harvard.edu/

[4] We use the Fe I and Fe II abundances defined as $A(\rm FeI) = \log_{10}\left(\frac{N_{\rm FeI}}{N_{\rm H}}\right)$ and $A(\rm FeII) = \log_{10}\left(\frac{N_{\rm FeII}}{N_{\rm H}}\right)$, respectively.

[5] Here the Li abundance is defined as $A(\rm Li) = \log_{10}\left(\frac{N_{\rm Li}}{N_{\rm H}}\right) - 12.00$.

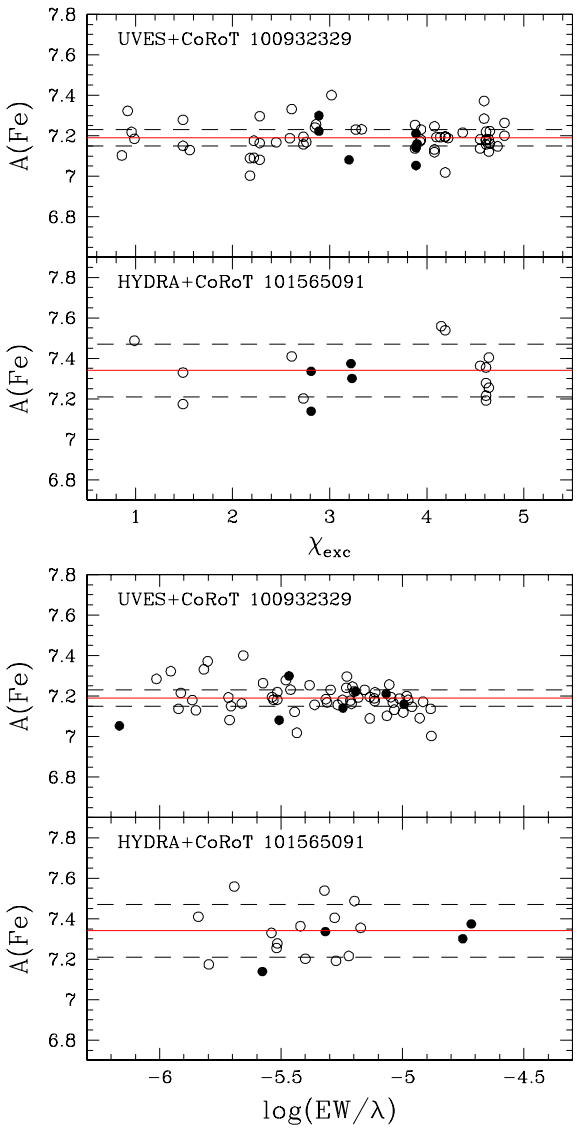

Fig. 4. *Upper panels*: ionization equilibrium for the targets 100932329 (UVES star) and 101565091 (Hydra star). *Lower panels*: equilibrium of the A(Fe)s and their EWs. Open and filled circles represent the abundances of Fe I (A(FeI)) and Fe II (A(FeII)), respectively. Red and black dashed lines represent the mean value of A(Fe) and standard deviation, respectively.

The Fig. 6 shows how the errors in the stellar parameters impact in the A(Li). In this context, the measurements of A(Li) for Hydra stars present errors higher than those found for the UVES stars. Nevertheless, we should be cautious with the Hydra data due, in particular, to the spectral resolution ($R \sim 15\,000$) associated with the observations.

4. Results

The computed stellar parameters, including rotational velocities $v \sin(i)$ and lithium abundances, for the present stellar sample are listed in Table 7. Figure 7 presents the corresponding Hertzsprung-Russell (HR) diagram, with the stars segregated by their Galactic locations (CoRoT center/anticenter) and iron abundances. In the bottom panel, stars are divided in three different groups using their [Fe/H] values[6]. Errors in the parameters

[6] [Fe/H] is calculated as in Canto Martins et al. (2011) using a solar iron abundance $A(\mathrm{Fe})_{\odot} = 7.49$ dex.

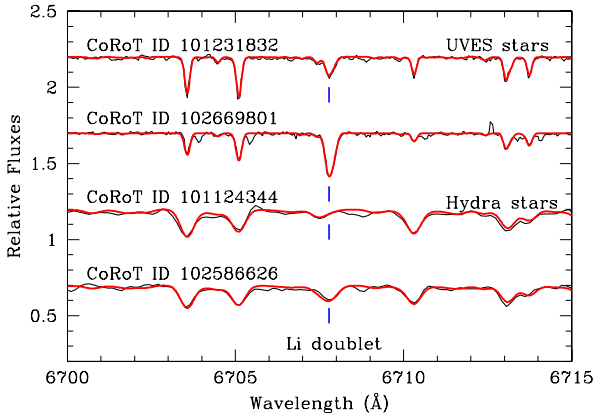

Fig. 5. Profile fitting of the Li doublet at ~6708 Å is shown for two UVES stars (CoRoT ID 101231832 and 102669801) and two Hydra stars (CoRoT ID 101124344 and 102586626). The observed spectra are presented using black lines, whereas the synthetic spectra are shown in red. The position of the Li doublet is indicated with a blue vertical line.

are also included in these panels. The magnitude of these errors is linked to the quality of the spectra, including spectral resolution R and S/N, and intrinsic effects of the stellar surfaces (i.e., high $v \sin(i)$, molecular bands in cool stars, etc.). Figure 7 shows that the present sample is comprised of stars in different evolutionary stages, ranging from the main sequence (MS) to the red giant branch (RGB).

We used the evolutionary tracks of Girardi et al. (2000) for different masses and metallicities[7] to identify the evolutionary stages of the stars in our sample. For this purpose, we identified the turn-off and the base of the RGB from the evolutionary tracks for each Z to define the MS, subgiant branch (SGB), and RGB regions. The results of this classification are listed in Table 7. Mean values for the stellar parameters and their respectives standard deviations corresponding to different CoRoT fields and evolutionary stages are given in Table 8.

Figure 7 also shows that the stellar evolutionary distribution for LRc01 and LRa01 CoRoT fields agrees with Deleuil et al. (2009). Furthermore, the relation between the color and evolutionary status is linked to the stellar metallicity. In fact, as we can see in Fig. 8 and Table 8, the distributions of $\log(g)$ for both fields are different and these differences correlate with the [Fe/H] distributions. Most LRa01 stars have $\log(g) \geq 3.75$ dex (~64%), whereas the LRc01 stars are spread along a large interval of $\log(g)$ and most of them have $\log(g) \leq 3.75$ dex. Combining this with the fact that the peaks of the [Fe/H] distributions and their mean values (Table 8) are different from one another, we can see that there is a relation between temperature, surface gravity, and evolutionary stage in the CoRoT fields considered here. While one might be tempted to associate these differences to selection effects, we note that these results agree with the recent spectroscopic survey of the CoRoT fields presented by G10. This point is discussed further in Sect. 4.4.

4.1. Comparison with previous results

To verify our results, we compared them with the results presented in G10. Only 11 stars of our sample were also analyzed

[7] For the different [Fe/H] groups, we used evolutionary tracks with a representative Z. Specifically, we used metallic abundances $Z = 0.004$, 0.019 and 0.030 for the group with [Fe/H] ≤ -0.25, $-0.25 <$ [Fe/H] $\leq +0.25$ and [Fe/H] $\geq +0.25$, respectively.

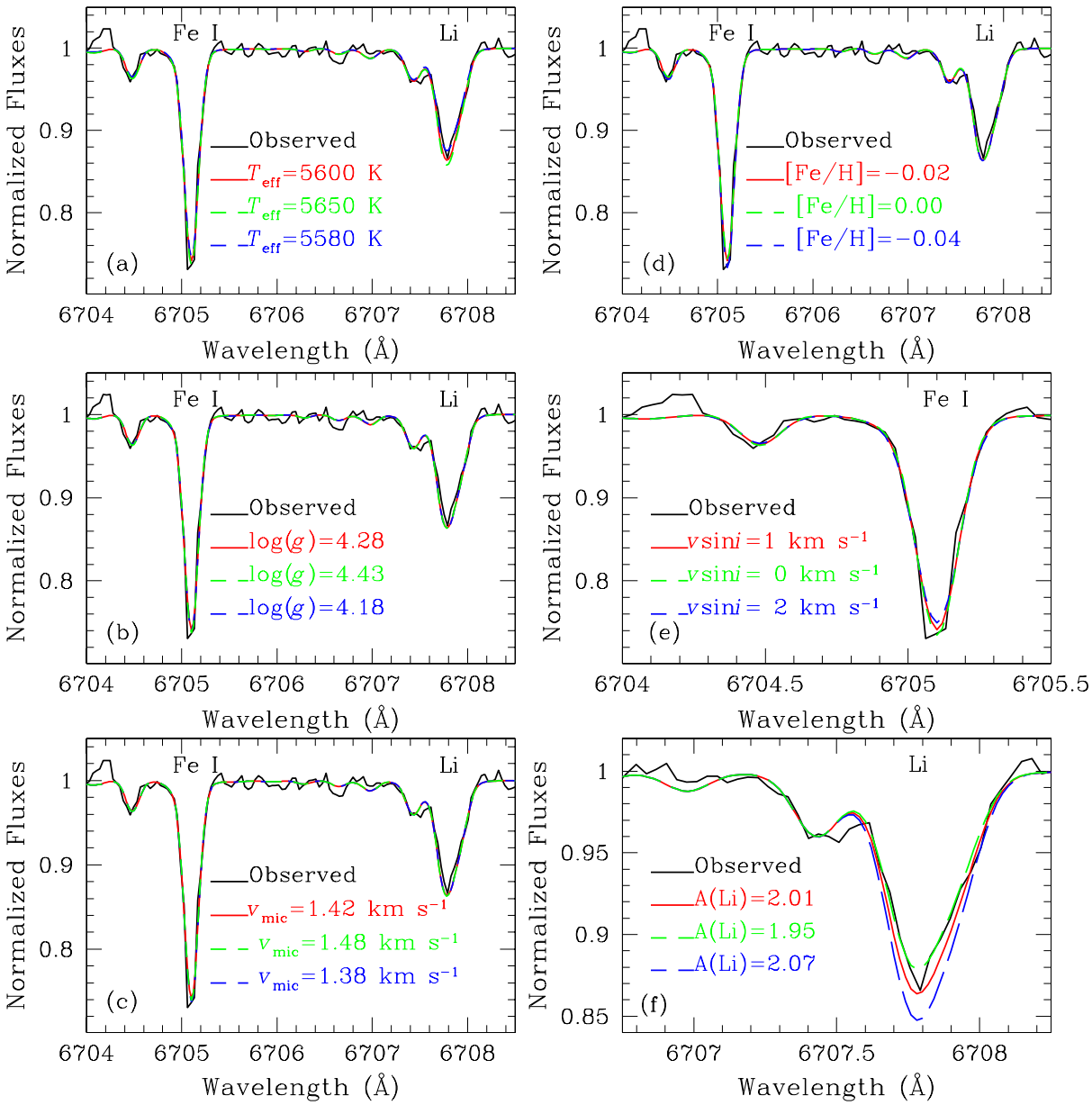

Fig. 6. As in Fig. 5, for the CoRoT ID 101231832 the profile fitting of an Fe I line and the Li doublet are presented. The panels **a)**, **b)**, **c)**, and **d)** show how the errors in each stellar parameter impact the computed synthetic spectra, which were used to measure $v \sin(i)$ (panel **e)**) and A(Li) (panel **f)**), and their respective errors. For all panels, the observed spectrum is presented using a black line, whereas the synthetic spectrum, computed with the derived stellar parameters, is presented using a red line. The dashed green and blue lines represent the computed synthetic spectra with errors for a given stellar parameter.

by G10. These stars are listed in Table 9. In Fig. 9 we plot the comparison between our results and the G10 findings. Our results agree with the survey of G10, with $T_{\rm eff}$, $\log(g)$ and $v \sin(i)$ presenting only small differences for most of the stars. However, star 101538522 presents a large dispersion in the $\log(g)$ values, which may be explained because of the quality of the data of G10 for a RGB star ($S/N \sim 23$). We cannot directly compare their derived abundances with ours since G10 report only the global metallicity ([M/H]), whereas here we present the iron abundance ([Fe/H]).

4.2. Radial and rotational velocities

Figure 10 shows the distribution of the measurements of barycentric radial velocity $v_{\rm rad}$ and rotational velocity $v \sin(i)$ listed in Tables 7 and 8. Small, but significant, differences are observed in the $v_{\rm rad}$ distribution for stars located in the Galactic center and anticenter directions. The percentages of stars with $v_{\rm rad} \leq 0$ km s^{-1} associated with the Galactic center and anticenter directions are 64% and 50%, respectively. In spite of the incompleteness of the sample, this behavior agrees with the $v_{\rm rad}$ distribution determined by G10 (see their Fig. 2).

In Fig. 10, small differences are also observed in the distribution of $v \sin(i)$ values. In fact, 68% and 42% of stars in the LRc01 and LRa01 fields present $v \sin(i) \leq 5$ km s^{-1}, respectively. The difference disapears quickly for stars with $v \sin(i) \leq 10$ km s^{-1}, where the percentage for both fields are similar (89% and 83% for LRc01 and LRa01 fields, respectively). A few high rotation values can be noticed among stars in the Galactic center region. While we caution that these distributions are affected to

Table 7. Stellar parameters for the stars in our sample.

CoRoT ID	$T_{\rm eff}(B-V)$ (K)	$T_{\rm eff}(J-K)$ (K)	$T_{\rm eff}$ (K)	$\log(g)$ (dex)	$v_{\rm mic}$ (km s^{-1})	[Fe/H] (dex)	Fe lines Fe I, Fe II	A(Li) (dex)	$v \sin(i)$ km s^{-1}	$v_{\rm rad}$ km s^{-1}	$E(B-V)$ (mag)	$E(J-K)$ (mag)	Evol. status	Inst
Main sequence stars														
100931549	5078	5571	5870^{+105}_{-90}	$4.08^{+0.13}_{-0.13}$	$1.65^{+0.09}_{-0.09}$	-0.16 ± 0.04	53, 7	1.96 ± 0.12	2^{+1}_{-1}	−68.2	0.28	0.04	MS	UVES
101057962	4082	3886	4640^{+120}_{-110}	$4.54^{+0.49}_{-0.49}$	$1.68^{+0.42}_{-0.36}$	0.25 ± 0.15	15, 4	-0.30 ± 0.16	3^{+2}_{-2}	41.3	0.30	0.21	MS	HYDRA
101128747	5125	6161	6395^{+65}_{-115}	$4.11^{+0.25}_{-0.26}$	$1.74^{+0.13}_{-0.11}$	0.24 ± 0.06	54, 5	3.21 ± 0.12	10^{+1}_{-1}	−30.8	0.39	0.03	MS	UVES
101204408	3946	3886	6335^{+54}_{-54}	$4.05^{+0.28}_{-0.28}$	$1.88^{+0.20}_{-0.29}$	-0.11 ± 0.04	50, 11	1.75 ± 0.07	5^{+1}_{-1}	9.2	1.02	0.55	MS	UVES
101208246	4809	5167	5530^{+30}_{-30}	$4.44^{+0.16}_{-0.15}$	$1.08^{+0.12}_{-0.12}$	0.28 ± 0.04	61, 6	1.11 ± 0.03	1^{+1}_{-1}	−70.4	0.30	0.06	MS	UVES
101231832	5050	5571	5600^{+50}_{-20}	$4.28^{+0.15}_{-0.10}$	$1.42^{+0.06}_{-0.04}$	-0.02 ± 0.02	61, 7	2.01 ± 0.06	1^{+1}_{-1}	−14.4	0.20	0.00	MS	UVES
101319580	4115	4323	4650^{+140}_{-190}	$3.95^{+0.48}_{-0.42}$	$3.97^{+0.93}_{-0.59}$	0.06 ± 0.15	17, 3	1.03 ± 0.35	10^{+2}_{-2}	41	0.29	0.08	MS	HYDRA
101455904	4973	5263	5230^{+370}_{-280}	$4.68^{+0.40}_{-0.30}$	$0.55^{+0.90}_{-0.55}$	0.09 ± 0.18	18, 4	2.01 ± 0.53	2^{+2}_{-2}	−4.9	0.10	0.00	MS	HYDRA
101462309	5065	5852	5880^{+35}_{-57}	$4.14^{+0.22}_{-0.20}$	$1.56^{+0.09}_{-0.10}$	0.14 ± 0.03	57, 9	2.43 ± 0.05	3^{+1}_{-1}	42.2	0.28	0.00	MS	UVES
101476063	4909	5167	5780^{+60}_{-55}	$4.40^{+0.14}_{-0.13}$	$1.44^{+0.07}_{-0.07}$	0.16 ± 0.03	60, 5	1.84 ± 0.07	2^{+1}_{-1}	−26	0.32	0.11	MS	UVES
101519854	4689	5413	5390^{+120}_{-90}	$4.79^{+0.16}_{-0.17}$	$2.90^{+0.40}_{-0.40}$	-0.05 ± 0.05	13, 3	1.37 ± 0.18	3^{+2}_{-2}	61.5	0.31	0.00	MS	HYDRA
101612300	4687	5167	6050^{+160}_{-200}	$4.90^{+0.47}_{-0.47}$	$0.47^{+0.80}_{-0.40}$	0.10 ± 0.06	10, 4	1.75 ± 0.27	2^{+2}_{-2}	56.6	0.51	0.16	MS	HYDRA
101613938	5146	6161	6155^{+95}_{-40}	$4.00^{+0.17}_{-0.17}$	$1.65^{+0.12}_{-0.11}$	-0.10 ± 0.04	51, 5	2.27 ± 0.08	5^{+2}_{-2}	−23.7	0.32	0.00	MS	UVES
102580280	5485	5465	5220^{+50}_{-190}	$4.52^{+0.16}_{-0.21}$	$1.38^{+1.14}_{-0.48}$	0.20 ± 0.08	16, 5	...[a]	16^{+3}_{-3}	57.8	...[b]	...[c]	MS	HYDRA
102585563	4700	4393	5637^{+38}_{-37}	$4.53^{+0.37}_{-0.36}$	$1.63^{+0.10}_{-0.10}$	-0.01 ± 0.04	54, 7	1.62 ± 0.05	6^{+1}_{-1}	0.3	0.39	0.27	MS	UVES
102585613	6528	6646	6194^{+276}_{-58}	$4.25^{+0.24}_{-0.24}$	$1.99^{+0.23}_{-0.30}$	-0.04 ± 0.05	51, 5	2.59 ± 0.22	9^{+1}_{-1}	−22.5	...[b]	...[c]	MS	UVES
102589564	6281	6646	6220^{+80}_{-65}	$3.90^{+0.28}_{-0.17}$	$1.65^{+0.48}_{-0.63}$	-0.05 ± 0.05	50, 9	2.35 ± 0.09	10^{+1}_{-1}	−51.5	...[b]	...[c]	MS	UVES
102591896	6134	6646	6330^{+80}_{-85}	$3.99^{+0.33}_{-0.27}$	$2.14^{+0.24}_{-0.34}$	-0.02 ± 0.07	53, 10	1.55 ± 0.07	7^{+1}_{-1}	−28.4	0.04	...[c]	MS	UVES
102603174	6044	6293	6200^{+46}_{-61}	$3.99^{+0.18}_{-0.29}$	$2.18^{+0.22}_{-0.24}$	-0.16 ± 0.05	50, 10	1.49 ± 0.03	8^{+1}_{-1}	−81.7	0.03	...[c]	MS	UVES
102604055	6453	6797	6397^{+229}_{-80}	$4.14^{+0.21}_{-0.21}$	$1.60^{+0.29}_{-0.24}$	-0.25 ± 0.06	54, 7	1.90 ± 0.16	9^{+1}_{-1}	−12.1	...[b]	...[c]	MS	UVES
102605405	5877	6226	6100^{+70}_{-134}	$3.99^{+0.27}_{-0.23}$	$1.53^{+0.09}_{-0.09}$	0.16 ± 0.04	50, 9	1.50 ± 0.23	7^{+1}_{-1}	−52.8	0.04	...[c]	MS	UVES
102611980	5725	6293	5890^{+35}_{-30}	$4.44^{+0.18}_{-0.24}$	$1.38^{+0.07}_{-0.07}$	0.01 ± 0.03	53, 10	2.37 ± 0.04	3^{+1}_{-1}	−21.1	0.04	...[c]	MS	UVES
102616719	5935	6430	6210^{+57}_{-50}	$4.30^{+0.24}_{-0.20}$	$1.66^{+0.20}_{-0.12}$	0.11 ± 0.05	58, 9	2.71 ± 0.06	6^{+1}_{-1}	−46.3	0.06	...[c]	MS	UVES
102618948	5672	6293	6110^{+45}_{-40}	$4.24^{+0.33}_{-0.38}$	$1.55^{+0.08}_{-0.08}$	0.38 ± 0.05	57, 10	1.30 ± 0.05	6^{+1}_{-1}	−5.2	0.11	...[c]	MS	UVES
102620828	5160	5167	5590^{+32}_{-35}	$4.31^{+0.25}_{-0.20}$	$0.86^{+0.08}_{-0.07}$	-0.18 ± 0.04	60, 7	...[a]	1^{+1}_{-1}	2.4	0.15	0.08	MS	UVES
102659670	6223	6797	6265^{+135}_{-165}	$3.89^{+0.38}_{-0.39}$	$0.84^{+0.26}_{-0.27}$	-0.09 ± 0.10	54, 4	1.63 ± 0.17	15^{+1}_{-1}	−76.1	0.00	...[c]	MS	UVES
102663892	5898	6293	6130^{+61}_{-69}	$4.35^{+0.20}_{-0.21}$	$1.36^{+0.10}_{-0.10}$	0.15 ± 0.04	61, 11	2.71 ± 0.08	3^{+1}_{-1}	−20.7	0.05	...[c]	MS	UVES
102669801	5682	6034	5960^{+65}_{-50}	$4.22^{+0.19}_{-0.23}$	$0.96^{+0.12}_{-0.20}$	-0.03 ± 0.06	55, 9	2.80 ± 0.09	3^{+1}_{-1}	−37.8	0.07	0.00	MS	UVES
102686019	6265	6646	6465^{+99}_{-176}	$4.12^{+0.34}_{-0.34}$	$1.15^{+0.28}_{-0.17}$	0.06 ± 0.06	54, 9	1.75 ± 0.15	12^{+1}_{-1}	−15.4	0.03	...[c]	MS	UVES
102687759	6033	6572	6390^{+70}_{-90}	$4.42^{+0.25}_{-0.25}$	$0.80^{+0.56}_{-0.24}$	-0.04 ± 0.06	52, 8	2.99 ± 0.09	5^{+1}_{-1}	−20.1	0.08	...[c]	MS	UVES
102692093	5870	5972	5870^{+50}_{-40}	$4.41^{+0.14}_{-0.14}$	$1.89^{+0.20}_{-0.26}$	-0.12 ± 0.05	54, 4	2.77 ± 0.06	8^{+1}_{-1}	−55.2	0.08	...[c]	MS	UVES
102705076	5414	5312	5620^{+360}_{-360}	$4.69^{+0.56}_{-0.48}$	$0.91^{+0.61}_{-0.61}$	0.04 ± 0.17	15, 3	1.44 ± 0.63	11^{+2}_{-2}	41.7	0.06	0.05	MS	HYDRA
102718064	5459	5312	6386^{+106}_{-90}	$4.44^{+0.32}_{-0.32}$	$0.97^{+0.63}_{-0.20}$	0.18 ± 0.07	55, 6	3.03 ± 0.11	10^{+1}_{-1}	−63.8	0.24	0.18	MS	UVES
102730409	5782	6161	5720^{+270}_{-270}	$4.63^{+0.47}_{-0.47}$	$1.26^{+0.46}_{-0.46}$	0.14 ± 0.13	17, 4	2.29 ± 0.37	3^{+2}_{-2}	59.7	...[b]	...[c]	MS	HYDRA
102735621	5748	6226	5960^{+330}_{-290}	$4.57^{+0.49}_{-0.44}$	$2.28^{+0.68}_{-0.68}$	0.02 ± 0.16	14, 4	2.01 ± 0.38	1^{+2}_{-1}	12.1	0.05	...[c]	MS	HYDRA
102740367	5571	5912	5700^{+170}_{-160}	$4.36^{+0.28}_{-0.23}$	$0.83^{+0.40}_{-0.59}$	0.03 ± 0.11	15, 4	2.10 ± 0.23	12^{+2}_{-2}	16.9	0.03	...[c]	MS	HYDRA
102741215	5785	6226	6985^{+279}_{-185}	$4.27^{+0.55}_{-0.55}$	$0.59^{+0.37}_{-0.37}$	0.29 ± 0.13	54, 11	1.70 ± 0.14	17^{+1}_{-1}	22.8	0.28	0.10	MS	UVES
102768747	5772	5912	5570^{+230}_{-220}	$4.64^{+0.30}_{-0.30}$	$1.79^{+0.60}_{-0.50}$	-0.25 ± 0.12	14, 4	1.61 ± 0.31	9^{+2}_{-2}	42.3	...[b]	...[c]	MS	HYDRA

Notes. Refer to Sects. 3.3 and 4 for details. [(a)] The measurement of A(Li) can not be obtained from the spectrum. [(b)] Reddening values $E(B-V)$ can not be obtained since $T_{\rm eff} < T_{\rm eff}(B-V)$. [(c)] Reddening values $E(J-K)$ can not be obtained since $T_{\rm eff} < T_{\rm eff}(J-K)$.

Table 7. continued.

CoRoT ID	$T_{\rm eff}(B-V)$ (K)	$T_{\rm eff}(J-K)$ (K)	$T_{\rm eff}$ (K)	$\log(g)$ (dex)	$v_{\rm mic}$ (km s^{-1})	[Fe/H] (dex)	Fe lines Fe I, Fe II	A(Li) (dex)	$v \sin(i)$ km s^{-1}	$v_{\rm rad}$ km s^{-1}	$E(B-V)$ (mag)	$E(J-K)$ (mag)	Evol. status	Inst
102789493	4618	4538	5600^{+150}_{-150}	$4.86^{+0.26}_{-0.22}$	$2.65^{+0.80}_{-0.80}$	0.25 ± 0.08	9, 4	...[a]	9^{+2}_{-2}	35.1	0.42	0.23	MS	HYDRA
102789962	6236	6875	6380^{+700}_{-700}	$4.76^{+0.54}_{-0.54}$	$1.67^{+0.90}_{-0.90}$	0.11 ± 0.14	13, 4	...[a]	10^{+2}_{-2}	27.6	0.03	...[c]	MS	HYDRA
Subgiant branch stars														
100532655	4976	5231	5550^{+50}_{-20}	$3.95^{+0.12}_{-0.12}$	$1.20^{+0.05}_{-0.07}$	0.28 ± 0.03	59, 8	1.41 ± 0.08	1^{+1}_{-1}	−36.8	0.22	0.06	SGB	UVES
100537408	5153	5552	5420^{+110}_{-390}	$1.60^{+0.36}_{-0.38}$	$0.83^{+0.46}_{-0.70}$	-0.92 ± 0.11	45, 5	1.45 ± 0.46	12^{+1}_{-1}	23.6	0.08	...[c]	SGB	UVES
100932329	4823	4776	5580^{+65}_{-70}	$3.66^{+0.18}_{-0.12}$	$1.85^{+0.23}_{-0.24}$	-0.30 ± 0.04	56, 7	2.10 ± 0.09	2^{+1}_{-1}	−83.6	0.31	0.19	SGB	UVES
101041358	5054	4916	5750^{+85}_{-60}	$4.10^{+0.24}_{-0.25}$	$1.69^{+0.18}_{-0.44}$	-0.33 ± 0.04	59, 4	2.04 ± 0.10	3^{+1}_{-1}	5.6	0.24	0.18	SGB	UVES
101043867	5162	5455	6190^{+85}_{-63}	$3.74^{+0.28}_{-0.24}$	$2.07^{+0.12}_{-0.13}$	0.19 ± 0.06	59, 10	1.55 ± 0.04	5^{+1}_{-1}	−18.2	0.32	0.13	SGB	UVES
101056542	5659	6041	6190^{+85}_{-65}	$3.82^{+0.21}_{-0.21}$	$2.05^{+0.17}_{-0.13}$	0.20 ± 0.06	59, 9	1.37 ± 0.11	3^{+2}_{-2}	−18.2	0.14	0.02	SGB	UVES
101076647	5050	5409	5905^{+130}_{-105}	$3.13^{+0.18}_{-0.18}$	$1.73^{+0.41}_{-0.09}$	-0.03 ± 0.04	56, 4	2.92 ± 0.15	8^{+1}_{-1}	−58	0.30	0.09	SGB	UVES
101102758	4840	4953	5760^{+25}_{-25}	$4.00^{+0.12}_{-0.16}$	$1.73^{+0.09}_{-0.11}$	0.04 ± 0.03	60, 7	1.94 ± 0.04	2^{+1}_{-1}	−99.7	0.35	0.17	SGB	UVES
101124344	4411	4494	4800^{+110}_{-110}	$2.05^{+0.36}_{-0.37}$	$1.52^{+0.31}_{-0.31}$	-0.19 ± 0.14	18, 4	0.25 ± 0.10	4^{+2}_{-2}	11.3	0.20	0.08	SGB	HYDRA
101249643	5420	5503	5760^{+150}_{-240}	$4.07^{+0.35}_{-0.32}$	$2.46^{+0.81}_{-0.81}$	-0.12 ± 0.13	13, 4	...[a]	22^{+4}_{-4}	21.9	0.10	0.04	SGB	HYDRA
101358013	5153	5189	5600^{+150}_{-140}	$2.30^{+0.38}_{-0.35}$	$2.05^{+0.70}_{-0.70}$	-0.50 ± 0.14	12, 4	2.27 ± 0.21	25^{+4}_{-4}	10.6	0.15	0.08	SGB	HYDRA
101411168	4084	4086	4980^{+190}_{-200}	$1.85^{+0.63}_{-0.60}$	$2.02^{+1.00}_{-0.33}$	-0.11 ± 0.21	17, 4	0.23 ± 0.32	9^{+3}_{-2}	−48.2	0.48	0.29	SGB	HYDRA
101478005	4855	4916	5135^{+20}_{-35}	$4.17^{+0.13}_{-0.13}$	$0.91^{+0.17}_{-0.07}$	0.09 ± 0.04	59, 5	0.06 ± 0.05	2^{+1}_{-1}	−37.4	0.11	0.05	SGB	UVES
101549180	5232	5409	5180^{+200}_{-200}	$4.12^{+0.42}_{-0.39}$	$0.56^{+1.00}_{-0.56}$	-0.34 ± 0.14	13, 3	2.08 ± 0.35	30^{+3}_{-3}	4.8	...[b]	...[c]	SGB	HYDRA
101562508	4165	4086	4760^{+100}_{-120}	$1.37^{+0.42}_{-0.40}$	$1.56^{+0.22}_{-0.18}$	-0.24 ± 0.09	14, 4	0.70 ± 0.30	2^{+2}_{-2}	−18.5	0.32	0.23	SGB	HYDRA
101565091	4881	5231	5690^{+160}_{-140}	$4.05^{+0.37}_{-0.32}$	$1.91^{+0.99}_{-0.99}$	-0.15 ± 0.13	15, 4	2.41 ± 0.21	1^{+2}_{-1}	−36	0.31	0.09	SGB	HYDRA
101565378	5284	5455	5770^{+200}_{-110}	$2.89^{+0.41}_{-0.33}$	$1.95^{+0.47}_{-0.33}$	-0.34 ± 0.14	50, 9	1.41 ± 0.18	12^{+1}_{-1}	−96.2	0.16	0.05	SGB	UVES
101599646	5128	5409	5730^{+250}_{-170}	$3.03^{+0.50}_{-0.53}$	$1.96^{+0.58}_{-0.58}$	-0.19 ± 0.09	12, 4	...[a]	18^{+3}_{-3}	−20.4	0.20	0.06	SGB	HYDRA
101600807	3886	4063	4550^{+160}_{-180}	$1.44^{+0.66}_{-0.59}$	$1.67^{+0.26}_{-0.21}$	-0.25 ± 0.14	14, 4	-0.15 ± 0.42	6^{+2}_{-2}	−43.2	0.36	0.17	SGB	HYDRA
101627005	4883	5363	5830^{+250}_{-220}	$3.69^{+0.38}_{-0.38}$	$1.92^{+0.70}_{-0.66}$	-0.04 ± 0.12	13, 3	1.67 ± 0.33	12^{+2}_{-2}	−9.9	0.35	0.08	SGB	HYDRA
101697676	5287	5503	6050^{+240}_{-100}	$3.87^{+0.26}_{-0.27}$	$1.99^{+0.39}_{-0.28}$	-0.11 ± 0.07	54, 7	2.49 ± 0.23	13^{+1}_{-1}	−43.3	0.23	0.09	SGB	UVES
102574603	5980	5757	5650^{+80}_{-40}	$3.00^{+0.03}_{-0.03}$	$1.73^{+0.32}_{-0.23}$	-0.28 ± 0.02	14, 4	2.08 ± 0.09	3^{+2}_{-2}	−12.8	...[b]	...[c]	SGB	HYDRA
102598042	5302	5274	5800^{+330}_{-380}	$3.84^{+0.37}_{-0.41}$	$0.77^{+0.53}_{-0.77}$	0.45 ± 0.15	15, 4	1.29 ± 0.54	1^{+2}_{-1}	−24.1	0.15	0.10	SGB	HYDRA
102602960	5772	5552	5480^{+50}_{-80}	$4.22^{+0.13}_{-0.06}$	$2.90^{+0.55}_{-0.37}$	-0.12 ± 0.04	18, 4	2.18 ± 0.11	4^{+2}_{-2}	58.2	...[b]	...[c]	SGB	HYDRA
102606185	6048	6041	6185^{+103}_{-116}	$3.80^{+0.14}_{-0.14}$	$2.02^{+0.11}_{-0.26}$	0.23 ± 0.05	61, 10	1.70 ± 0.14	10^{+1}_{-1}	−42.7	0.03	0.02	SGB	UVES
102612876	4333	4063	4790^{+50}_{-50}	$1.77^{+0.07}_{-0.10}$	$1.65^{+0.14}_{-0.10}$	-0.55 ± 0.03	13, 3	0.50 ± 0.15	3^{+2}_{-2}	42.2	0.24	0.25	SGB	HYDRA
102614844	5198	5409	5445^{+25}_{-50}	$4.14^{+0.25}_{-0.19}$	$1.00^{+0.06}_{-0.07}$	0.37 ± 0.04	58, 4	0.93 ± 0.06	1^{+1}_{-1}	−3.7	0.07	0.00	SGB	UVES
102615343	6103	6101	6110^{+250}_{-230}	$3.65^{+0.11}_{-0.11}$	$0.56^{+1.89}_{-0.56}$	0.14 ± 0.12	13, 5	2.43 ± 0.30	10^{+2}_{-2}	58.5	0.00	0.00	SGB	HYDRA
102627939	5362	5455	5550^{+240}_{-260}	$3.90^{+0.47}_{-0.22}$	$2.02^{+0.24}_{-0.24}$	0.07 ± 0.06	17, 4	...[a]	7^{+2}_{-2}	66	0.06	0.01	SGB	HYDRA
102637778	5640	5455	5550^{+100}_{-100}	$3.42^{+0.19}_{-0.20}$	$2.13^{+0.52}_{-1.78}$	-0.12 ± 0.07	18, 3	1.35 ± 0.15	3^{+2}_{-2}	5.3	...[b]	0.01	SGB	HYDRA
102654716	6079	5867	5750^{+55}_{-50}	$3.25^{+0.42}_{-0.41}$	$0.59^{+0.30}_{-0.26}$	-0.10 ± 0.06	51, 5	2.23 ± 0.08	6^{+1}_{-1}	−14	...[b]	...[c]	SGB	UVES
102657182	5338	5318	5525^{+25}_{-45}	$4.18^{+0.16}_{-0.16}$	$1.37^{+0.19}_{-0.13}$	-0.03 ± 0.04	61, 8	1.05 ± 0.02	2^{+1}_{-1}	−67.9	0.06	0.03	SGB	UVES
102658181	5520	5503	5655^{+28}_{-23}	$3.81^{+0.14}_{-0.14}$	$1.28^{+0.04}_{-0.05}$	0.12 ± 0.04	56, 4	2.01 ± 0.03	1^{+1}_{-1}	−72.2	0.03	0.02	SGB	UVES
102669038	6436	6101	6105^{+105}_{-125}	$3.46^{+0.28}_{-0.28}$	$0.81^{+0.32}_{-0.19}$	-0.14 ± 0.09	54, 5	1.20 ± 0.13	10^{+1}_{-1}	−49.6	...[b]	0.00	SGB	UVES

Table 7. continued.

CoRoT ID	$T_{\rm eff}(B-V)$ (K)	$T_{\rm eff}(J-K)$ (K)	$T_{\rm eff}$ (K)	$\log(g)$ (dex)	$v_{\rm mic}$ (km s^{-1})	[Fe/H] (dex)	Fe lines Fe I, Fe II	A(Li) (dex)	$v \sin(i)$ km s^{-1}	$v_{\rm rad}$ km s^{-1}	$E(B-V)$ (mag)	$E(J-K)$ (mag)	Evol. status	Inst
102676872	4881	4677	5539^{+103}_{-107}	$3.18^{+0.27}_{-0.15}$	$1.75^{+0.14}_{-0.22}$	-0.07 ± 0.05	60, 7	1.40 ± 0.14	11^{+1}_{-1}	−28.1	0.26	0.21	SGB	UVES
102678564	6228	6164	5900^{+459}_{-212}	$3.46^{+0.56}_{-0.73}$	$3.57^{+1.60}_{-1.63}$	-0.71 ± 0.17	46, 8	1.55 ± 0.32	17^{+1}_{-1}	−4.6	…[b]	…[c]	SGB	UVES
102679796	6286	6164	6170^{+65}_{-55}	$3.40^{+0.27}_{-0.22}$	$1.77^{+0.32}_{-0.27}$	-0.45 ± 0.05	41, 4	1.70 ± 0.06	5^{+1}_{-1}	−61.5	…[b]	0.00	SGB	UVES
102695542	4673	4645	5520^{+210}_{-190}	$1.99^{+0.46}_{-0.47}$	$2.06^{+0.37}_{-0.27}$	-0.11 ± 0.15	14, 3	…[a]	12^{+3}_{-3}	46.4	0.37	0.21	SGB	HYDRA
102705009	5653	5652	5510^{+370}_{-340}	$3.91^{+0.51}_{-0.50}$	$1.03^{+0.53}_{-0.51}$	0.13 ± 0.15	15, 4	1.48 ± 0.53	4^{+2}_{-2}	0.7	…[b]	…[c]	SGB	HYDRA
102709247	5362	5601	5570^{+38}_{-38}	$4.00^{+0.14}_{-0.12}$	$0.91^{+0.16}_{-0.05}$	0.30 ± 0.03	53, 10	1.67 ± 0.04	1^{+1}_{-1}	−22.9	0.06	0.00	SGB	UVES
102728377	5953	5652	5820^{+180}_{-170}	$3.11^{+0.26}_{-0.25}$	$1.16^{+0.22}_{-0.21}$	-0.10 ± 0.10	15, 4	2.28 ± 0.21	8^{+2}_{-2}	35	…[b]	0.02	SGB	HYDRA
102738854	5799	5867	5840^{+80}_{-25}	$4.05^{+0.24}_{-0.24}$	$1.37^{+0.08}_{-0.11}$	0.03 ± 0.04	57, 5	1.65 ± 0.05	4^{+1}_{-1}	−91.9	0.00	0.00	SGB	UVES
102740520	5320	5601	5640^{+35}_{-32}	$3.81^{+0.12}_{-0.12}$	$1.28^{+0.14}_{-0.06}$	0.35 ± 0.04	52, 7	2.49 ± 0.04	4^{+1}_{-1}	3.9	0.10	0.00	SGB	UVES
102743491	5234	5274	5990^{+170}_{-120}	$3.36^{+0.40}_{-0.43}$	$1.63^{+0.58}_{-0.41}$	0.51 ± 0.06	11, 4	1.20 ± 0.25	4^{+2}_{-2}	40.6	0.23	0.13	SGB	HYDRA
102743929	4596	4302	5330^{+250}_{-250}	$4.03^{+0.20}_{-0.20}$	$2.65^{+0.36}_{-0.36}$	-0.11 ± 0.09	10, 4	1.25 ± 0.42	5^{+2}_{-2}	25.6	0.34	0.29	SGB	HYDRA
102758371	6056	5981	5710^{+130}_{-130}	$4.01^{+0.18}_{-0.18}$	$1.83^{+0.21}_{-0.20}$	-0.17 ± 0.07	14, 3	2.39 ± 0.17	9^{+2}_{-2}	39.9	…[b]	…[c]	SGB	HYDRA
102764866	5789	5552	5775^{+70}_{-91}	$3.35^{+0.34}_{-0.32}$	$1.01^{+0.28}_{-0.56}$	-0.41 ± 0.05	53, 7	…[a]	17^{+1}_{-1}	−20.1	0.00	0.04	SGB	UVES
102772347	5701	5552	5970^{+90}_{-90}	$3.41^{+0.21}_{-0.33}$	$1.58^{+0.23}_{-0.09}$	0.02 ± 0.06	55, 10	2.40 ± 0.11	10^{+1}_{-1}	−23.8	0.07	0.07	SGB	UVES
102625766	5987	5757	5690^{+120}_{-150}	$3.00^{+0.14}_{-0.15}$	$1.60^{+0.75}_{-0.63}$	-0.23 ± 0.06	14, 4	1.36 ± 0.16	10^{+2}_{-2}	4.7	…[b]	…[c]	SGB	HYDRA
Red giant branch stars														
101066444	2877	3714	4640^{+120}_{-130}	$2.72^{+0.72}_{-0.67}$	$2.94^{+0.60}_{-0.29}$	0.11 ± 0.25	11, 4	0.58 ± 0.16	6^{+2}_{-2}	12	0.68	0.38	RGB	HYDRA
101154362	4246	4155	4620^{+170}_{-130}	$0.16^{+0.70}_{-0.70}$	$1.28^{+0.18}_{-0.18}$	-0.39 ± 0.22	14, 4	…[a]	3^{+2}_{-2}	−29.8	0.20	0.16	RGB	HYDRA
101165983	4148	3999	4200^{+100}_{-100}	$1.69^{+0.28}_{-0.34}$	$1.34^{+0.09}_{-0.08}$	-0.16 ± 0.09	13, 4	…[a]	4^{+2}_{-2}	−44	0.00	0.07	RGB	HYDRA
101178248	4013	3957	4460^{+120}_{-220}	$2.11^{+0.41}_{-0.42}$	$2.37^{+0.31}_{-0.24}$	-0.23 ± 0.14	12, 4	0.85 ± 0.28	4^{+2}_{-2}	13	0.24	0.19	RGB	HYDRA
101237841	4039	3821	4210^{+80}_{-70}	$2.48^{+0.28}_{-0.23}$	$1.88^{+0.07}_{-0.07}$	-0.34 ± 0.08	16, 4	…[a]	1^{+2}_{-1}	64.2	0.07	0.16	RGB	HYDRA
101258619	4358	4302	4950^{+170}_{-80}	$3.10^{+0.22}_{-0.20}$	$2.25^{+0.18}_{-0.14}$	-0.04 ± 0.08	18, 4	0.49 ± 0.14	7^{+2}_{-2}	−17.3	0.31	0.20	RGB	HYDRA
101268962	4358	4302	4870^{+180}_{-240}	$2.97^{+0.37}_{-0.42}$	$2.20^{+0.41}_{-0.27}$	-0.29 ± 0.15	16, 4	0.20 ± 0.53	1^{+2}_{-1}	11.4	0.27	0.17	RGB	HYDRA
101305750	4406	4494	4780^{+70}_{-130}	$2.65^{+0.60}_{-0.63}$	$0.98^{+0.10}_{-0.10}$	0.31 ± 0.19	14, 4	0.30 ± 0.41	6^{+2}_{-2}	0.8	0.19	0.08	RGB	HYDRA
101346995	3540	3766	3840^{+150}_{-210}	$2.19^{+0.46}_{-0.56}$	$1.15^{+0.15}_{-0.15}$	0.49 ± 0.11	11, 4	…[a]	3^{+2}_{-2}	39.8	0.09	0.01	RGB	HYDRA
101347642	4090	4178	4300^{+190}_{-350}	$0.31^{+0.40}_{-0.40}$	$1.10^{+0.18}_{-0.10}$	-0.25 ± 0.14	13, 4	-0.55 ± 0.64	5^{+2}_{-2}	−52.3	0.10	0.03	RGB	HYDRA
101347760	4489	4355	4880^{+200}_{-80}	$2.39^{+0.24}_{-0.24}$	$3.87^{+0.72}_{-0.72}$	-0.82 ± 0.06	12, 3	…[a]	4^{+2}_{-2}	−30.1	0.20	0.16	RGB	HYDRA
101392071	3473	3697	4140^{+240}_{-240}	$0.48^{+0.87}_{-0.87}$	$1.97^{+0.36}_{-0.36}$	-0.74 ± 0.12	13, 4	…[a]	1^{+2}_{-1}	−39.6	0.26	0.20	RGB	HYDRA
101421386	4371	4227	4640^{+120}_{-130}	$1.88^{+0.58}_{-0.58}$	$1.38^{+0.48}_{-0.48}$	-0.75 ± 0.14	16, 4	0.22 ± 0.28	1^{+2}_{-1}	−79.2	0.14	0.13	RGB	HYDRA
101422730	4137	4063	4410^{+210}_{-230}	$1.31^{+0.45}_{-0.49}$	$2.31^{+0.65}_{-0.47}$	-0.46 ± 0.16	13, 4	0.30 ± 0.56	5^{+2}_{-2}	28.8	0.14	0.12	RGB	HYDRA
101423629	3999	4020	4460^{+200}_{-210}	$2.87^{+0.58}_{-0.55}$	$1.45^{+0.29}_{-0.36}$	0.14 ± 0.16	17, 4	…[a]	5^{+2}_{-2}	−34.3	0.25	0.16	RGB	HYDRA
101433432	4031	4108	4230^{+330}_{-250}	$1.30^{+0.50}_{-0.55}$	$1.68^{+0.24}_{-0.20}$	-0.37 ± 0.16	14, 4	-0.05 ± 0.66	1^{+2}_{-1}	−33.5	0.09	0.03	RGB	HYDRA
101451115	4182	3999	4780^{+140}_{-110}	$3.41^{+0.29}_{-0.27}$	$2.68^{+0.66}_{-0.38}$	-0.29 ± 0.07	14, 3	1.97 ± 0.24	3^{+2}_{-2}	32	0.32	0.28	RGB	HYDRA
101458937	3951	3897	4330^{+210}_{-150}	$3.07^{+0.43}_{-0.40}$	$2.52^{+0.40}_{-0.46}$	-0.18 ± 0.14	15, 3	…[a]	4^{+2}_{-2}	−18.4	0.20	0.17	RGB	HYDRA
101461526	3696	3714	4480^{+210}_{-200}	$2.77^{+0.53}_{-0.57}$	$2.39^{+0.50}_{-0.50}$	-0.24 ± 0.17	18, 4	-0.20 ± 0.05	5^{+2}_{-2}	−34.5	0.40	0.33	RGB	HYDRA
101464585	3449	3664	4190^{+210}_{-120}	$1.15^{+0.84}_{-0.85}$	$3.06^{+0.49}_{-0.38}$	-0.88 ± 0.10	13, 4	-0.45 ± 0.39	6^{+2}_{-2}	−81.4	0.29	0.24	RGB	HYDRA
101479386	3966	4042	4380^{+200}_{-200}	$3.29^{+0.66}_{-0.67}$	$2.59^{+0.50}_{-0.46}$	-0.13 ± 0.17	13, 4	-0.20 ± 0.43	6^{+2}_{-2}	−0.6	0.22	0.12	RGB	HYDRA
101483826	4095	4178	4790^{+110}_{-120}	$0.95^{+0.41}_{-0.45}$	$1.95^{+1.05}_{-0.59}$	-0.50 ± 0.12	14, 4	…[a]	6^{+2}_{-2}	−41.5	0.39	0.20	RGB	HYDRA

Table 7. continued.

CoRoT ID	$T_{\rm eff}(B-V)$ (K)	$T_{\rm eff}(J-K)$ (K)	$T_{\rm eff}$ (K)	$\log(g)$ (dex)	$v_{\rm mic}$ (km s^{-1})	[Fe/H] (dex)	Fe lines Fe I, Fe II	A(Li) (dex)	$v\sin(i)$ km s^{-1}	$v_{\rm rad}$ km s^{-1}	$E(B-V)$ (mag)	$E(J-K)$ (mag)	Evol. status	Inst
101489251	3013	3585	4150^{+170}_{-160}	$2.78^{+0.50}_{-0.56}$	$2.71^{+0.41}_{-0.33}$	0.00 ± 0.16	14, 4	-0.78 ± 0.36	5^{+2}_{-2}	−38.9	0.36	0.28	RGB	HYDRA
101489977	3961	4086	4450^{+170}_{-120}	$2.94^{+0.34}_{-0.36}$	$2.35^{+0.27}_{-0.23}$	0.02 ± 0.10	13, 3	0.25 ± 0.23	5^{+2}_{-2}	−25.8	0.26	0.13	RGB	HYDRA
101492953	4328	4155	4900^{+240}_{-120}	$2.42^{+0.22}_{-0.22}$	$1.73^{+0.50}_{-0.50}$	-0.25 ± 0.09	15, 4	0.65 ± 0.39	4^{+2}_{-2}	1.8	0.30	0.24	RGB	HYDRA
101536086	4181	4202	4720^{+150}_{-250}	$3.47^{+0.48}_{-0.53}$	$2.10^{+0.43}_{-0.43}$	-0.04 ± 0.11	16, 4	0.63 ± 0.31	7^{+2}_{-2}	10.3	0.29	0.17	RGB	HYDRA
101538522	3696	3731	4180^{+210}_{-120}	$1.81^{+0.24}_{-0.24}$	$1.63^{+0.17}_{-0.22}$	-0.28 ± 0.08	12, 4	-0.70 ± 0.47	3^{+2}_{-2}	−89.1	0.22	0.20	RGB	HYDRA
101550759	4077	4042	4570^{+190}_{-190}	$2.65^{+0.45}_{-0.47}$	$1.95^{+0.32}_{-0.26}$	-0.08 ± 0.16	16, 4	0.21 ± 0.40	1^{+2}_{-1}	−32.5	0.27	0.19	RGB	HYDRA
101552742	4287	4227	4740^{+340}_{-170}	$3.00^{+0.44}_{-0.45}$	$3.29^{+0.82}_{-0.82}$	-0.36 ± 0.11	12, 4	-0.30 ± 0.72	9^{+2}_{-2}	17.2	0.24	0.17	RGB	HYDRA
101555541	4192	4108	4760^{+80}_{-80}	$1.70^{+0.22}_{-0.22}$	$1.96^{+0.38}_{-0.26}$	-0.46 ± 0.08	14, 3	1.13 ± 0.18	5^{+2}_{-2}	−50.6	0.31	0.22	RGB	HYDRA
101561050	4031	3999	4240^{+130}_{-140}	$1.73^{+0.33}_{-0.31}$	$2.16^{+0.18}_{-0.16}$	-0.28 ± 0.10	12, 3	0.44 ± 0.33	3^{+2}_{-2}	−17.4	0.09	0.09	RGB	HYDRA
101569925	4065	4131	4520^{+220}_{-290}	$2.22^{+0.52}_{-0.72}$	$1.98^{+0.36}_{-0.36}$	-0.18 ± 0.17	14, 4	0.30 ± 0.60	4^{+2}_{-2}	38.4	0.24	0.13	RGB	HYDRA
101598546	3964	4202	4560^{+140}_{-170}	$2.87^{+0.53}_{-0.32}$	$2.47^{+0.24}_{-0.20}$	-0.20 ± 0.06	14, 4	0.26 ± 0.26	4^{+2}_{-2}	−27.5	0.33	0.12	RGB	HYDRA
101622447	3983	4108	4660^{+240}_{-230}	$2.57^{+0.25}_{-0.29}$	$2.35^{+0.43}_{-0.31}$	-0.31 ± 0.11	14, 4	0.33 ± 0.53	4^{+2}_{-2}	−4.8	0.38	0.19	RGB	HYDRA
101626971	4284	4277	5050^{+140}_{-130}	$3.17^{+0.49}_{-0.47}$	$1.51^{+0.32}_{-0.26}$	-0.32 ± 0.12	20, 4	0.65 ± 0.18	1^{+2}_{-1}	48.1	0.40	0.23	RGB	HYDRA
101635594	3279	3917	3810^{+190}_{-150}	$2.26^{+0.50}_{-0.52}$	$1.89^{+0.25}_{-0.24}$	0.21 ± 0.17	13, 4	...[a]	6^{+2}_{-2}	7.3	0.14	...[c]	RGB	HYDRA
101642292	4045	4063	4500^{+100}_{-90}	$2.84^{+0.29}_{-0.29}$	$2.17^{+0.20}_{-0.18}$	-0.15 ± 0.07	14, 4	0.31 ± 0.16	4^{+2}_{-2}	−24.1	0.25	0.15	RGB	HYDRA
101665008	4079	4042	4490^{+70}_{-70}	$2.90^{+0.22}_{-0.22}$	$1.83^{+0.19}_{-0.17}$	-0.26 ± 0.07	15, 3	0.22 ± 0.14	7^{+2}_{-2}	−2.2	0.22	0.16	RGB	HYDRA
102586626	4406	4178	4920^{+60}_{-80}	$3.12^{+0.29}_{-0.21}$	$1.17^{+0.19}_{-0.15}$	-0.09 ± 0.06	53, 5	1.38 ± 0.12	3^{+2}_{-2}	72.4	0.27	0.24	RGB	HYDRA
102662415	4687	4523	4920^{+70}_{-150}	$3.71^{+0.19}_{-0.20}$	$1.69^{+0.31}_{-0.48}$	-0.06 ± 0.04	16, 3	0.25 ± 0.25	8^{+2}_{-2}	8.3	0.10	0.11	RGB	HYDRA
102694697	4403	4251	4680^{+100}_{-180}	$2.72^{+0.63}_{-0.53}$	$1.45^{+0.19}_{-0.19}$	-0.01 ± 0.12	16, 4	0.30 ± 0.18	5^{+2}_{-2}	43.4	0.14	0.14	RGB	HYDRA
102694848	4187	4063	4370^{+250}_{-320}	$0.69^{+0.91}_{-0.91}$	$1.39^{+0.23}_{-0.28}$	-0.51 ± 0.22	16, 4	0.00 ± 0.59	8^{+2}_{-2}	83.4	0.08	0.11	RGB	HYDRA
102697221	4440	4202	4770^{+80}_{-70}	$1.29^{+0.24}_{-0.26}$	$1.48^{+0.08}_{-0.08}$	-0.34 ± 0.06	16, 4	0.50 ± 0.19	5^{+2}_{-2}	4.7	0.17	0.18	RGB	HYDRA
102705308	4933	4709	5130^{+40}_{-50}	$3.07^{+0.17}_{-0.19}$	$1.53^{+0.06}_{-0.02}$	-0.34 ± 0.03	57, 8	0.20 ± 0.10	2^{+1}_{-1}	−21.4	0.08	0.10	RGB	UVES
102706020	4623	4355	4760^{+70}_{-70}	$1.23^{+0.39}_{-0.43}$	$1.55^{+0.15}_{-0.14}$	-0.77 ± 0.07	16, 4	0.00 ± 0.18	7^{+2}_{-2}	16.8	0.05	0.12	RGB	HYDRA
102754990	4511	4382	4790^{+70}_{-60}	$2.21^{+0.15}_{-0.18}$	$2.89^{+0.65}_{-0.67}$	-0.60 ± 0.06	14, 3	0.20 ± 0.14	5^{+2}_{-2}	81.7	0.13	0.12	RGB	HYDRA
102767494	5442	5455	5240^{+470}_{-290}	$3.58^{+0.44}_{-0.44}$	$2.39^{+0.46}_{-0.46}$	-0.26 ± 0.18	12, 4	...[a]	11^{+2}_{-2}	82.4	...[b]	...[c]	RGB	HYDRA
102769088	4455	4382	4790^{+120}_{-180}	$2.49^{+0.47}_{-0.40}$	$2.34^{+0.22}_{-0.22}$	-0.41 ± 0.10	15, 4	0.46 ± 0.47	5^{+2}_{-2}	−2.4	0.17	0.12	RGB	HYDRA
102792032	4428	4202	4690^{+110}_{-90}	$2.84^{+0.27}_{-0.27}$	$3.09^{+0.80}_{-0.50}$	-0.47 ± 0.09	17, 4	0.62 ± 0.22	7^{+2}_{-2}	27.7	0.12	0.16	RGB	HYDRA

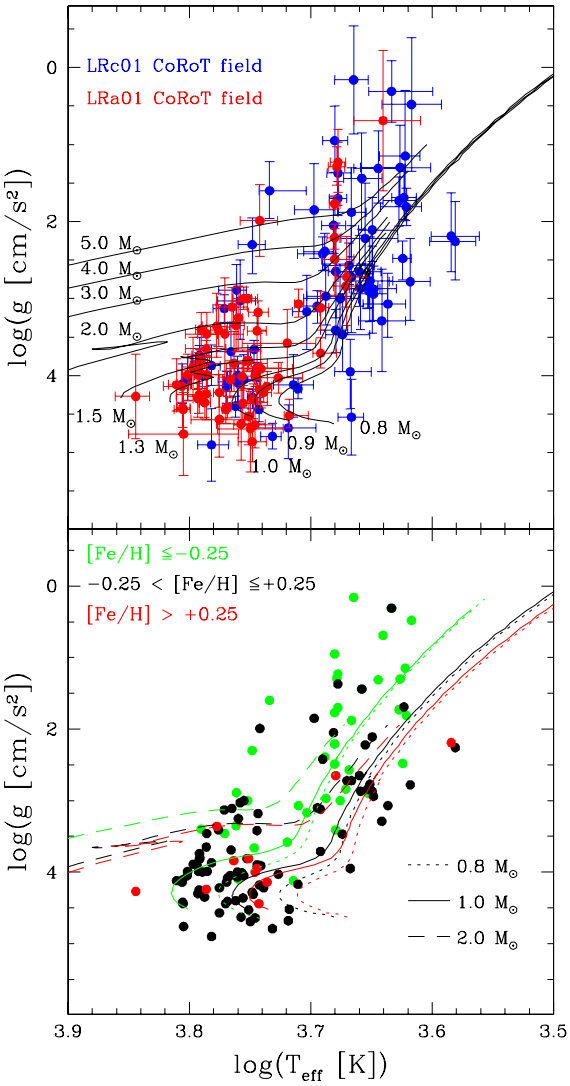

Fig. 7. *Upper panel*: HR diagram of the stellar sample segregated by Galactic direction (center/anticenter). Blue and red dots represent stars in the LRc01 and LRa01 fields, respectively. Evolutionary tracks for $Z = 0.019$, from Girardi et al. (2000), are shown for stellar masses between 0.8 and 5 $M_{\odot}$. *Lower panel*: HR diagram of the stellar sample segregated by the iron abundance [Fe/H]. Green, black, and red points represent stars with [Fe/H] ≤ -0.25, $-0.25 <$ [Fe/H] $\leq +0.25$ and [Fe/H] $\geq +0.25$, respectively. Evolutionary tracks for $Z = 0.004$, $Z = 0.019$, and $Z = 0.030$, from Girardi et al. (2000), are presented with lines in green, black, and red, respectively. In this panel, only the following stellar mass values are represented: 0.8 $M_{\odot}$ (dot lines), 1.0 $M_{\odot}$ (solid lines) and 2.0 $M_{\odot}$ (dash lines). For clarity, in *both panels* we plot only the evolutionary tracks until the RGB stage.

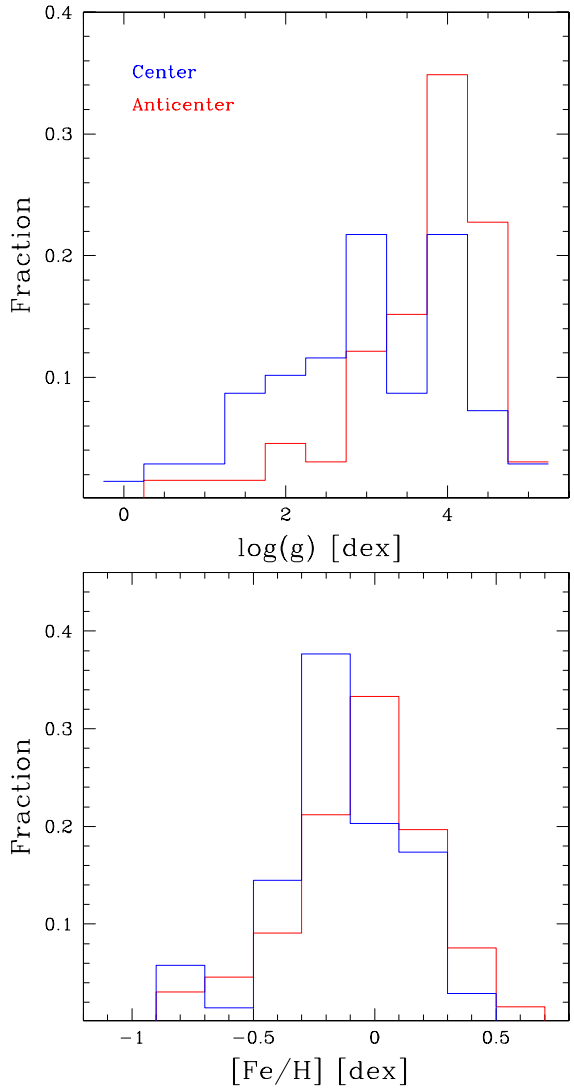

Fig. 8. *Upper panel*: histogram of the surface gravities $\log(g)$ in the CoRoT fields. *Lower panel*: histograms of the iron abundances [Fe/H] for the different evolutionary stages. A relation between [Fe/H] and evolutionary status is clearly present for the stars in our sample.

some degree by incompleteness, the observed behavior of the $v \sin(i)$ distribution in particular does follow the behavior expected for FGK stars (Soderblom 1983; De Medeiros et al. 1996; Nordström et al. 2004). In fact, as we can see from Fig. 11, which displays the individual $v \sin(i)$ values versus $T_{\rm eff}$, the rotational behavior for stars of the present stellar sample is rather well in agreement with the well-established behavior of rotation for stars evolving from the MS to red giant stages. Essentially, stars in the MS exhibit a wide range of rotational velocity values, which are related with the stellar masses and $T_{\rm eff}$. For these stars, the measured values of $v \sin(i)$ ranges from a few km s^{-1} to about 100 times the solar rotation rate, whereas the stars along the RGB are typically slow rotators, except for a few unusual cases presenting moderate to rapid rotation (Cortés et al. 2009; Carney et al. 2008, 2003; De Medeiros et al. 1996; De Medeiros & Mayor 1990).

4.3. Photometric temperatures and reddening

It is possible to evaluate the reddening effects along the two different Galactic directions by comparing the initial photometric temperatures, derived without taking reddening into account, and the final, spectroscopically-derived, and presumably reddening-insensitive temperatures. This analysis allows one to establish how the determination of physical parameters from photometric data is affected by neglecting reddening effects, to evaluate the error budget brought about by reddening, and also to check the presence of possible reddening gradients in the CoRoT windows. In this sense, the present $E(B-V)$ estimates for individual stars may assist follow-up programs of specific groups of stars, including for instance solar analogs and solar twins.

To accomplish this goal, we compare the photometric temperatures $T_{\rm eff}(B-V)$ and $T_{\rm eff}(J-K)$ and those derived from

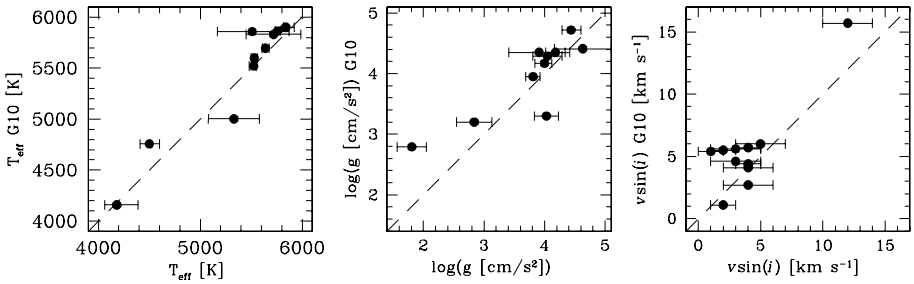

Fig. 9. Comparison between our results and the results of G10 for stars in common. Some differences can be noted, however, overall our result agree with G10.

Table 8. Mean parameters of the CoRoT fields.

	LRc01	LRa01
All evolutionary stages		
$T_{\rm eff}(B-V)$ [K]	4395 ± 595	5507 ± 631
$T_{\rm eff}(J-K)$ [K]	4558 ± 711	5562 ± 802
$T_{\rm eff}$ [K]	5008 ± 677	5693 ± 529
$\log(g)$ [dex]	2.91 ± 1.14	3.68 ± 0.88
[Fe/H] [dex]	−0.16 ± 0.28	−0.06 ± 0.27
$v_{\rm rad}$ [km s^{-1}]	−15.3 ± 38.3	−0.1 ± 43.7
$v \sin(i)$ [km s^{-1}]	6 ± 5	7 ± 4
A(Li) [dex]	0.96 ± 0.99	1.62 ± 0.79
$\langle E(B-V)\rangle$	0.27 ± 0.14	0.12 ± 0.11
$\langle E(J-K)\rangle$	0.14 ± 0.10	0.10 ± 0.09
Main sequence stars		
$T_{\rm eff}(B-V)$ [K]	4744 ± 426	5791 ± 460
$T_{\rm eff}(J-K)$ [K]	5199 ± 754	6041 ± 379
$T_{\rm eff}$ [K]	5654 ± 566	6041 ± 379
$\log(g)$ [dex]	4.34 ± 0.32	4.34 ± 0.26
[Fe/H] [dex]	0.07 ± 0.15	0.03 ± 0.16
$v_{\rm rad}$ [km s^{-1}]	−19.8 ± 32.5	5.2 ± 61.9
$v \sin(i)$ [km s^{-1}]	4 ± 3	8 ± 4
A(Li) [dex]	1.73 ± 0.83	2.10 ± 0.56
$\langle E(B-V)\rangle$	0.36 ± 0.22	0.11 ± 0.12
$\langle E(J-K)\rangle$	0.10 ± 0.15	0.13 ± 0.10
Subgiant branch stars		
$T_{\rm eff}(B-V)$ [K]	4923 ± 449	5594 ± 532
$T_{\rm eff}(J-K)$ [K]	5097 ± 537	5512 ± 533
$T_{\rm eff}$ [K]	5532 ± 466	5699 ± 293
$\log(g)$ [dex]	3.19 ± 1.00	3.52 ± 0.59
[Fe/H] [dex]	−0.16 ± 0.27	−0.04 ± 0.29
$v_{\rm rad}$ [km s^{-1}]	−53.9 ± 35.2	23.1 ± 66.1
$v \sin(i)$ [km s^{-1}]	9 ± 8	7 ± 5
A(Li) [dex]	1.48 ± 0.89	1.67 ± 0.54
$\langle E(B-V)\rangle$	0.25 ± 0.11	0.12 ± 0.13
$\langle E(J-K)\rangle$	0.11 ± 0.07	0.07 ± 0.09
Redgiant branch stars		
$T_{\rm eff}(B-V)$ [K]	3984 ± 369	4592 ± 340
$T_{\rm eff}(J-K)$ [K]	4040 ± 212	4427 ± 385
$T_{\rm eff}$ [K]	4497 ± 295	4824 ± 232
$\log(g)$ [dex]	2.28 ± 0.87	2.45 ± 1.00
[Fe/H] [dex]	−0.24 ± 0.29	−0.35 ± 0.24
$v_{\rm rad}$ [km s^{-1}]	−68.0 ± 35.7	85.4 ± 48.7
$v \sin(i)$ [km s^{-1}]	4 ± 2	6 ± 3
A(Li) [dex]	0.25 ± 0.57	0.39 ± 0.40
$\langle E(B-V)\rangle$	0.25 ± 0.12	0.13 ± 0.06
$\langle E(J-K)\rangle$	0.17 ± 0.08	0.14 ± 0.04

our spectroscopic analysis, $T_{\rm eff}$. We determined the photometric temperatures, at the beginning, using the luminosity class from the CoRoTSky database. For some stars, however, the physical

Table 9. Common stars with Gazzano et al. (2010).

ID	Our work $T_{\rm eff}$ K	Our work $\log(g)$ [dex]	Our work $v \sin(i)$ km s^{-1}	Gazzano et al. (2010) $T_{\rm eff}$ K	Gazzano et al. (2010) $\log(g)$ [dex]	Gazzano et al. (2010) $v \sin(i)$ km s^{-1}
101102758	5760	4.00	2.0	5865	4.17	1.1
101208246	5530	4.44	1.0	5600	4.72	5.4
101538522	4180	1.81	3.0	4159	2.79	4.6
101642292	4500	2.84	4.0	4757	3.20	4.1
102657182	5525	4.18	2.0	5521	4.35	5.5
102705009	5510	3.91	4.0	5858	4.35	2.7
102730409	5720	4.63	3.0	5832	4.41	5.6
102738854	5840	4.05	4.0	5901	4.29	5.7
102740367	5700	4.36	12.0	...	...	15.7
102740520	5640	3.81	4.0	5696	3.95	4.4
102743929	5330	4.03	5.0	5002	3.30	6.0

parameters provide a new classification of luminosity class for which new photometric temperatures were computed using this information. The photometric temperatures are listed in Table 7, including those derived using a new luminosity class. Finally, in Figs. 12 and 13, we present the comparisons between our spectroscopic $T_{\rm eff}$ values and the photometric estimations $T_{\rm eff}(B-V)$ and $T_{\rm eff}(J-K)$.

Figure 12 shows that the stars in CoRoT run LRc01 present larger differences between $T_{\rm eff}(B-V)$ and $T_{\rm eff}$ than those in run LRa01, which can be expected because of the higher extinction levels in the Galactic center direction. In fact, for this color index, $(B-V)$, the percentages of CoRoT stars presenting differences up to 200, 500, and 800 K in the Galactic center direction are 6%, 42%, and 81%, respectively. The percentages of CoRoT stars presenting the same temperature differences in the Galactic anticenter direction are 38%, 86%, and 92%, respectively. To obtain a reddening estimation for the LRc01 and LRa01 CoRoT fields, we used the calibration of Flower (1996; corrected by Torres 2010), which give us $T_{\rm eff}(B-V)$ and $T_{\rm eff}$, assuming the latter (spectroscopically derived) as being the actual value. This assumption is valid because $T_{\rm eff}$ is not affected by reddening. As such, for a star with a solar value $(B-V)_\odot$, we estimated reddening levels ($E(B-V)$) of about 0.06, 0.17, and 0.30, for the differences of 200, 500, and 800 K, respectively. Similarly, for an RGB star with a $(B-V)_0 \sim 1.6$, these differences in temperature represent reddening levels of about $E(B-V) \sim 0.07$, 0.16, and 0.20, respectively.

We also derived $E(B-V)$ values for individual targets using their values of $T_{\rm eff}(B-V)$ and $T_{\rm eff}$ of Table 7. These values are given in Table 7. Table 8 shows the mean values $\langle E(B-V)\rangle$. Then, for all evolutionary stages, $\langle E(B-V)\rangle \sim 0.27 \pm 0.14$ and 0.12 ± 0.11 for the LRc01 and LRa01 fields, respectively. These mean values are somewhat influenced by the distributions of temperature and evolutionary stage in each field. Then

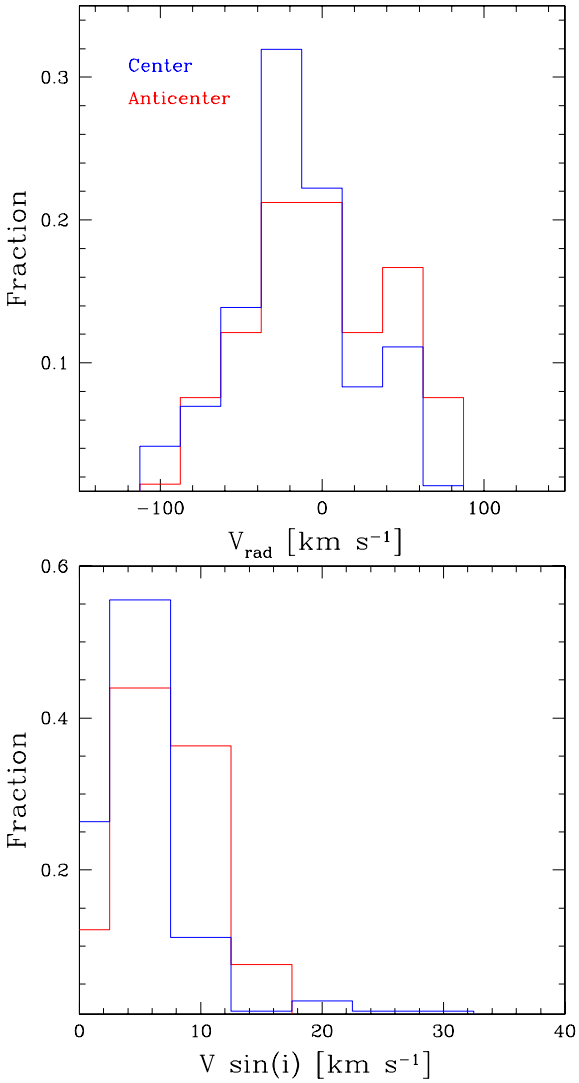

Fig. 10. *Upper panel*: histograms of the radial velocity $v_{\rm rad}$ for the LRc01 (blue line) and LRa01 (red line) fields. *Lower panel*: histograms of the rotational velocity $v \sin(i)$ for the LRc01 (blue line) and LRa01 (red line) fields.

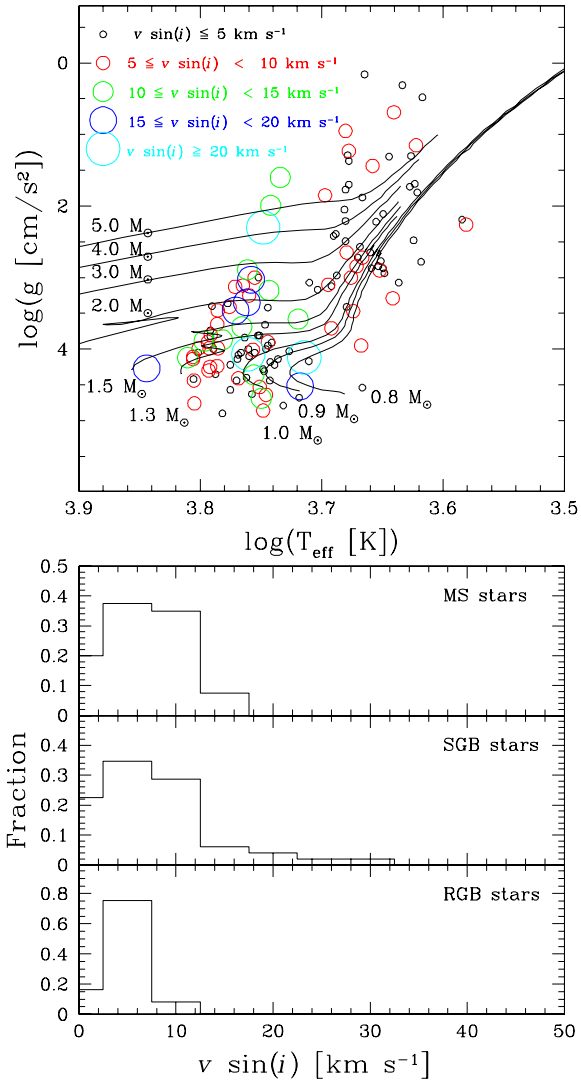

Fig. 11. *Upper panel*: distribution of $v \sin(i)$ for the stars in our sample along the HR diagram. Symbol size is proportional to the $v \sin(i)$ value. Evolutionary tracks are defined as in Fig. 7. *Lower panels*: histograms of the rotational velocity $v \sin(i)$ for the different evolutionary stages.

we computed mean values $\langle E(B-V)\rangle$ for each evolutionary stage for both fields. For the LRc01 field, $E\langle(B-V)\rangle$ levels are of 0.36 ± 0.22, 0.25 ± 0.11, and 0.25 ± 0.12 for MS, SGB and RGB stars, respectively, whereas for the LRa01 field, $\langle E(B-V)\rangle$ levels are of 0.11 ± 0.12, 0.12 ± 0.13, and 0.13 ± 0.06 for MS, SGB, and RGB stars, respectively.

On the other hand, there are also differences when the $T_{\rm eff}(J-K)$ values are compared with $T_{\rm eff}$ in both CoRoT fields. The percentages of CoRoT stars presenting differences up to 200, 500, and 800 K in the Galactic center direction are 15%, 61%, and 90%, respectively. The percentages of CoRoT stars presenting the same temperature differences in the Galactic anticenter direction are 38%, 80%, and 91%, respectively.

The reddening levels for both CoRoT fields were determined using the relations of Alonso et al. (1996, 1999), which provide $T_{\rm eff}(J-K)$ and $T_{\rm eff}$, again assuming that the latter provides the correct value. As such, for a star with a solar value $(J-K)_\odot$, reddening levels are of about $E(J-K) \sim 0.04$, 0.09, and 0.16 for differences up to 200, 500, and 800 K, respectively. Similarly, for a RGB star with a $(J-K) \sim 1.0$ these differences in temperature imply a reddening of about $E(J-K) \sim 0.13$, 0.37, and 0.71.

Similar to $E(B-V)$, we also derived $E(J-K)$ values for individual targets using their values of $T_{\rm eff}(B-V)$ and $T_{\rm eff}$ of Table 7. These values are given in Table 7. Table 8 shows mean values $\langle E(J-K)\rangle$. Then, for all evolutionary stages, $\langle E(J-K)\rangle \sim 0.14 \pm 0.10$ and 0.10 ± 0.09 for the LRc01 and LRa01, respectively. For the LRc01 field, $\langle E(J-K)\rangle$ levels are of 0.10 ± 0.15, 0.11 ± 0.07, and 0.17 ± 0.08 for MS, SGB, and RGB stars, respectively, whereas for the LRa01 field $\langle E(J-K)\rangle$ levels are of 0.13 ± 0.10, 0.07 ± 0.09, and 0.14 ± 0.04 for MS, SGB, and RGB stars, respectively.

When we compare $\langle E(B-V)\rangle$ with $\langle E(J-K)\rangle$ for each field or the evolutionary stages in each field, typically they do not agree with one another. However, the dispersion in these mean values is very high, which could explain this discrepancy.

In contrast, the mean reddening values show that the LRc01 field is more affected by reddening than the LRa01 field. In fact, we used the reddening maps of Schlafly & Finkbeiner (2011) and Schlegel et al. (1998), and the Galactic Extinction Calculator[8] of

[8] Available in the NED web page http://ned.ipac.caltech.edu/forms/calculator.html

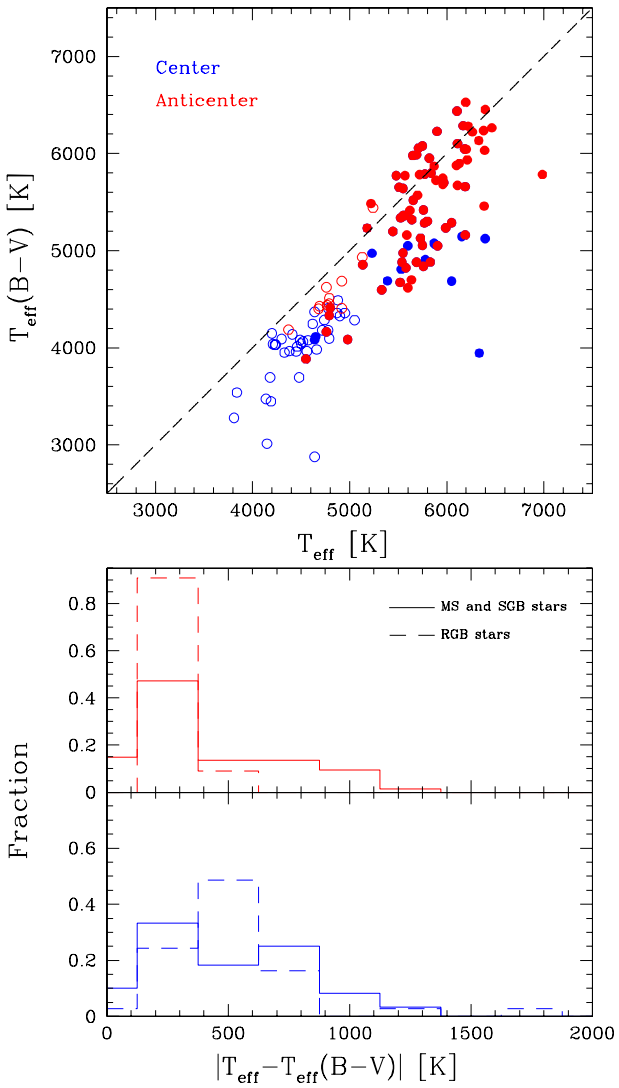

Fig. 12. *Upper panel*: differences between photometric $T_{\rm eff}(B-V)$ and spectroscopic $T_{\rm eff}$ for stars in the LRc01 (open and filled blue dots) and LRa01 (filled and open red dots) CoRoT fields. Filled circles represent MS and SGB stars, whereas open circles represent RGB stars. *Lower panels*: histograms of the difference between photometric $T_{\rm eff}(B-V)$ and spectroscopic $T_{\rm eff}$ for the stars in the LRc01 (blue line) and LRa01 (red line) CoRoT fields.

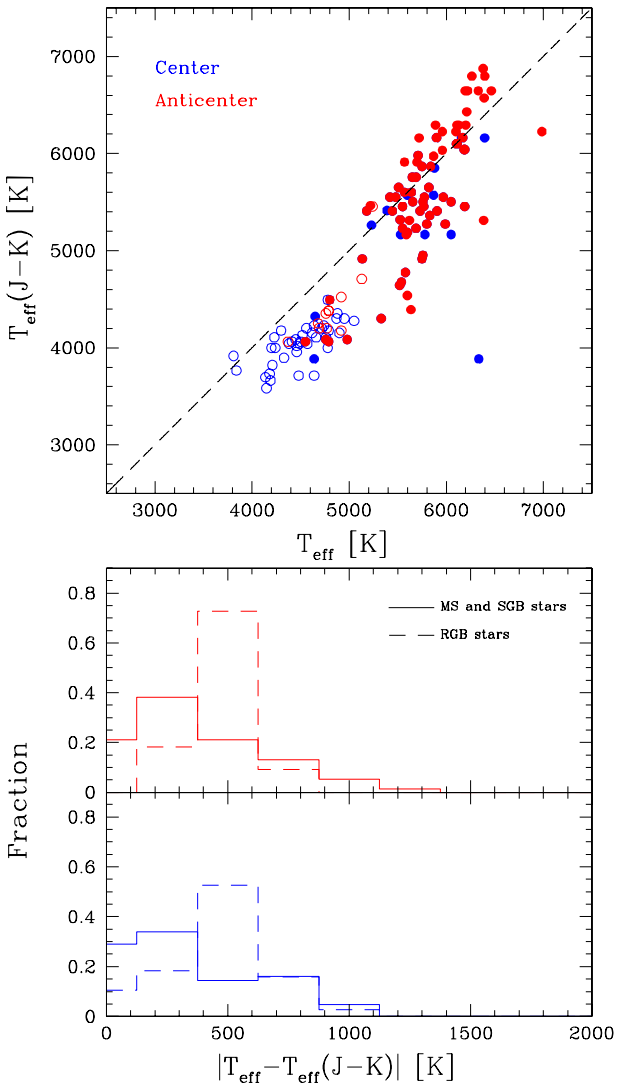

Fig. 13. *Upper panel*: differences between photometric $T_{\rm eff}(J-K)$ and spectroscopic $T_{\rm eff}$ for the stars in the LRc01 (open and filled blue dots) and LRa01 (filled and open red dots) CoRoT fields. Filled circles represent MS and SGB stars, whereas open circles represent RGB stars. *Lower panels*: histograms of the difference between photometric $T_{\rm eff}(J-K)$ and spectroscopic $T_{\rm eff}$ for the stars in the LRc01 (blue line) and LRa01 (red line) CoRoT fields.

the NASA/IPAC Extragalactic Database (NED) to obtain mean values of reddening of the LRc01 and LRa01 fields. However, NED only provides reliable reddening values for the LRc01 field. The reddening values of Schlafly & Finkbeiner (2011) and Schlegel et al. (1998) agree with the present work. Specifically, for the LRc01 field Schlafly & Finkbeiner (2011) give reddening values $E(B-V) \sim 0.28$ and $E(J-K) \sim 0.13$, whereas Schlegel et al. (1998) give $E(B-V) \sim 0.30$ and $E(J-K) \sim 0.16$.

To make a comparison, we also obtained the color indices $(B-V)$ and $(J-K)$ for the stellar sample of G10. Again, we computed the $T_{\rm eff}(B-V)$ and $T_{\rm eff}(J-K)$ values for the stars for which those authors spectroscopically derived atmospheric parameters, and we obtained the differences between these temperatures and the spectroscopic temperatures. Histograms showing these differences for the stars in the LRc01 and LRa01 fields are presented in Fig. 14. There are some differences between these distribution and the corresponding histograms derived in Figs. 12 and 13. Compared to our sample, the G10 sample presents a greater proportion of highly-reddened stars in the Galactic center direction. In fact, for the $(B-V)$ color, the percentages of CoRoT stars presenting differences up to 200, 500, and 800 K in the Galactic center direction are 0%, 3%, and 30%, respectively. The percentages of CoRoT stars presenting the same temperature differences in the Galactic anticenter direction are 3%, 41%, and 80%, respectively.

This difference can probably be explained by the fact that the relative number of stars in the center and anticenter directions differs between the two studies. In addition, our sample size is only ∼10% the size of the G10 sample, and sample size-related biases can also affect this comparison accordingly.

Otherwise, those stars with both determinations $E(B-V)$ and $E(J-K)$, only 27% present consistent values ($E(B-V) \sim 0.5\ E(J-K)$), which can be produced by the errors in the photometry (see Sect. 3.3), and/or errors in determination of $T_{\rm eff}$ and their respective errors. Therefore, it is important to take these values with caution.

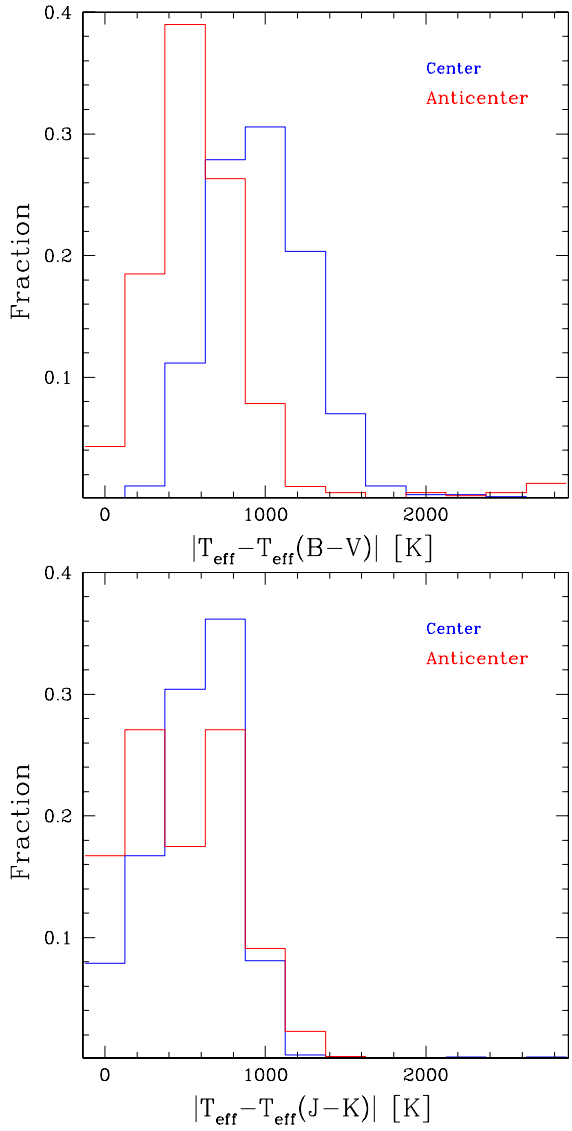

Fig. 14. *Upper panel*: histograms of the difference between photometric $T_{\rm eff}(B-V)$ and spectroscopic $T_{\rm eff}$ for the sample of Gazzano et al. (2010). *Lower panel*: histograms of the difference between photometric $T_{\rm eff}(J-K)$ and spectroscopic $T_{\rm eff}$ for the sample of Gazzano et al. (2010).

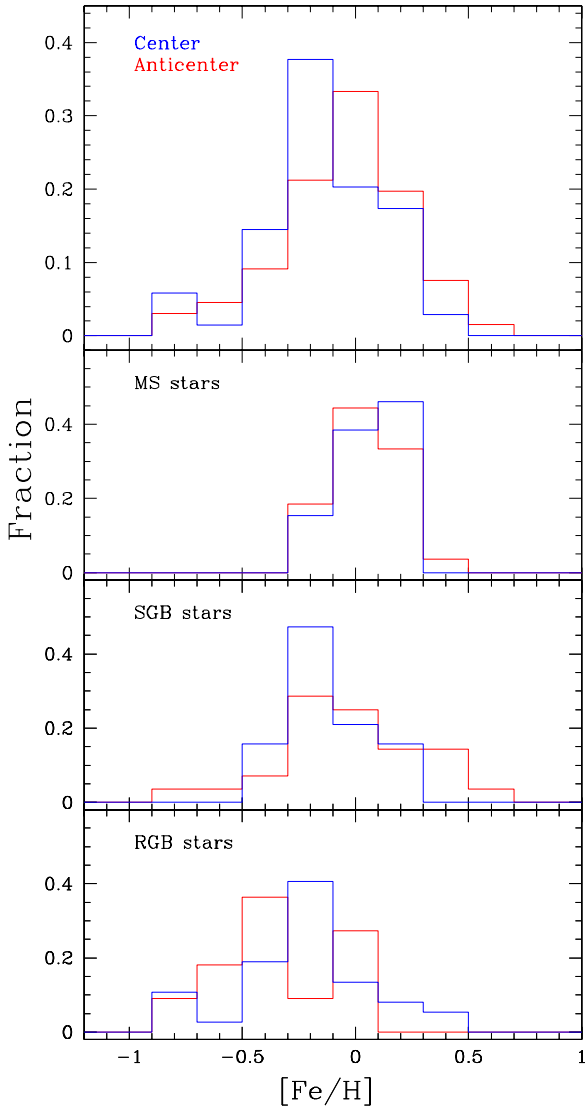

Fig. 15. *Upper panel*: histogram of the iron abundances [Fe/H] in the CoRoT fields. *Lower panels*: histograms of the iron abundances [Fe/H] for the different evolutionary stages. A relation between [Fe/H] and evolutionary status is clearly present for the stars in our sample.

4.4. The iron and Li abundances and three Li-rich giants

Figure 15 shows that our values of [Fe/H] strongly agree with typical values found in the Galactic disk, which range from −1.3 to +0.4 (Reddy et al. 2006; Bensby et al. 2007; Meléndez et al. 2008). In fact, as was mentioned before, differences are expected in the distributions of [Fe/H] between both CoRoT fields. As shown in Fig. 2, the LRc01 field is composed of stars with lower [Fe/H] values than the LRa01 field. Stars with [Fe/H] < 0.0 represent 75% and 56% of the sample in the LRc01 and LRa01 fields, respectively. Following this point, stars in those CoRoT fields also present important differences in the distribution of $T_{\rm eff}$, $\log(g)$, and evolutionary stages, suggesting a link with [Fe/H]. This can be seen when the histograms for each evolutionary stage are analyzed (see Fig. 15). The mean values of [Fe/H] for stars in the MS, SGB, and RGB of the LRc01 field are +0.05, −0.16, and −0.26, respectively. For the LRa01 field, the corresponding mean values are +0.04, −0.02, and −0.41.

Our [Fe/H] distributions show a similar behavior to that presented by Gazzano et al. (2010) in an extensive spectroscopic survey of the CoRoT field[9]. Similarly, our results show that most stars on the MS present solar [Fe/H] values, whereas most stars in evolved stages have low metallicities. The relation between [Fe/H], evolutionary stages, and the two different Galactic directions observed by CoRoT found in Gazzano et al. (2010), which we confirmed, could be explained by the metallicity gradient found in the Galactic disk (Pedicelli et al. 2009; Friel et al. 2010; Luck et al. 2011)[10].

The behavior of the lithium abundances for the stars in our sample is shown in Fig. 16, with the A(Li) distribution along the HR diagram in the upper panel and histograms for different evolutionary stages in the lower panel. The A(Li) measurements for

[9] We present measurements of [Fe/H], whereas G10 present the global metallicity [M/H]. The comparison should be done with caution since both quantities do not represent the same abundance.

[10] Our stellar sample comprises stars in early and evolved stages and they present a narrow interval in apparent magnitudes V, which implies a spread in absolute magnitudes and distances.

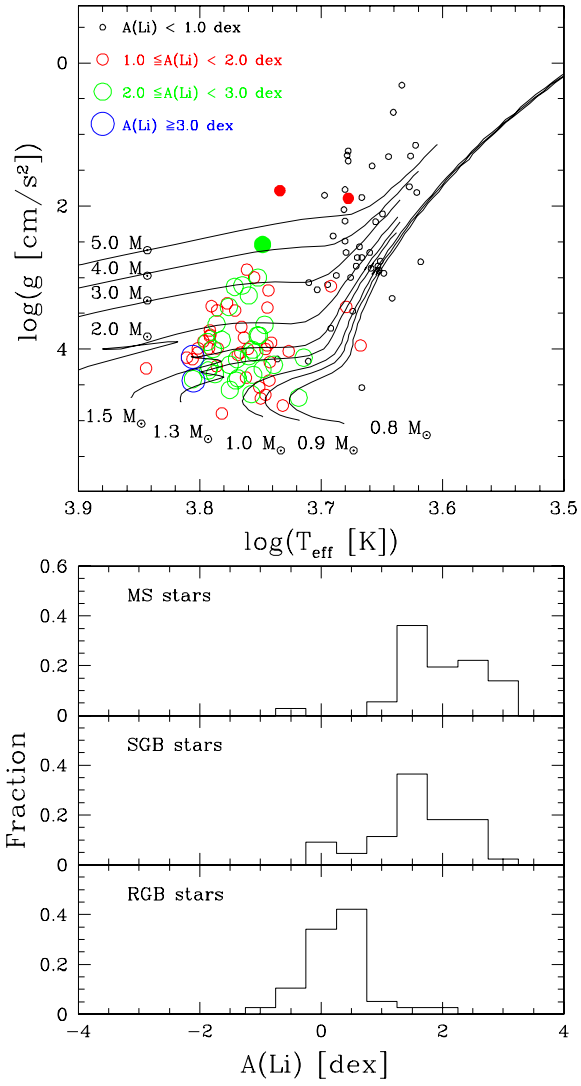

Fig. 16. *Upper panel*: distribution of A(Li) along the HR diagram for the stars of the present sample. Symbol size is proportional to the value of A(Li). The stars showing an abnormal lithium behavior are presented using filled circles. Evolutionary tracks are the same as in Fig. 7. *Lower panels*: histograms of A(Li) for different evolutionary stages.

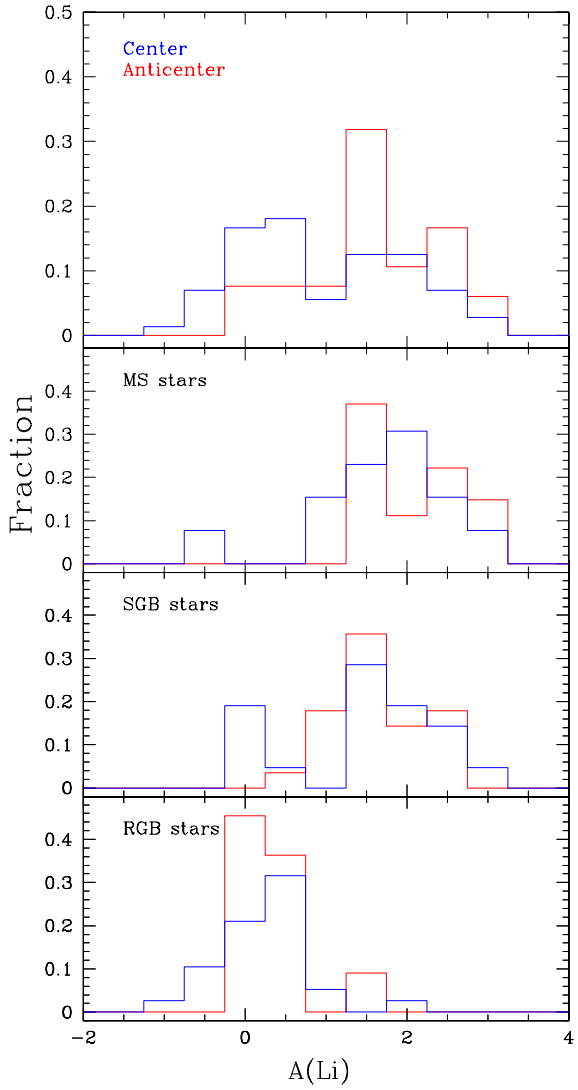

Fig. 17. *Upper panel*: histogram of the lithium abundances A(Li) in the CoRoT fields with stars segregated in the two Galactic directions, with blue indicating the Center and red the Anti-center. *Lower panels*: histograms of A(Li) for different evolutionary stages.

the present stellar sample clearly follows the well-established scenario for the lithium behavior at the referred evolutionary phases (Luck 1977; Boesgaard & Tripicco 1986; Soderblom et al. 1993; Wallerstein et al. 1994; De Medeiros et al. 1997; Lèbre et al. 1999; De Medeiros et al. 2000; Meléndez et al. 2010).

Indeed, the stellar lithium content is extremely sensitive to the physical conditions inside stars. As well established, the surface Li abundance is further depleted after stars leave the MS and undergo the first dredge-up (Iben 1967a,b). As a result, RGB stars essentially exhibit low A(Li) (Brown et al. 1989). Nevertheless, an increasing list of studies report the discovery of giant stars violating this rule (e.g., Wallerstein & Sneden 1982; Brown et al. 1989; Pilachowski et al. 2000; Martell & Shetrone 2013), the so-called lithium-rich giant stars, which present atypically large lithium abundances, in contrast to theoretical predictions. Three stars in the present CoRoT sample show an abnormal lithium behavior: CoRoT ID 100537408, with an A(Li) of 1.45 ± 0.46; CoRoT ID 101358013, with an A(Li) of 2.27 ± 0.21; and CoRoT ID 101555541, with an A(Li) of 1.13 ± 0.18 (see Fig. 16).

Figure 17 shows the distributions of A(Li) for the whole sample located in the Galactic center and anti-center directions. The upper panel of Fig. 17 provides an indication that a difference may be present, with the highest lithium content in the anti-center direction and an apparent bimodal distribution in the center direction. However, the histograms for the stars segregated by MS, SGB, and RGB evolutionary stages (bottom panel) show no statistically clear difference between Galactic center and anti-center. Indeed, the distributions of A(Li) for stars separated by evolutionary stages seem to indicate that the behavior of the lithium content observed along the HR diagram follows the same trend irrespective of the location of stars in Galactic center or anti-center directions.

5. Conclusions

We present physical parameters ($T_{\rm eff}$, $\log(g)$, $v_{\rm mic}$, and $v \sin(i)$), dynamical properties ($v_{\rm rad}$), and chemical abundances ([Fe/H] and A(Li)) for a sample of 138 stars stars located in the CoRoT exoplanet fields LRc01 and LRa01, based on observations collected with UVES/VLT at ESO and Hydra/Blanco at

CTIO. The derived parameters allow us to characterize physically the observed stellar sample, with the stars located in different regions of the HR diagram, from the MS to well-evolved stages, including the SGB and RGB. We also provide estimates of possible errors in the temperatures derived using photometric calibrations, and also of reddening values for the stars in the aforementioned CoRoT fields.

Our results show a relation between $T_{\rm eff}$, evolutionary stage, and [Fe/H] in the CoRoT fields, which is related to the color distributions in these fields. These results are in agreement with independent photometric and spectroscopic surveys of the CoRoT fields. These results give support to our spectroscopically-determined parameters. Our chemical analysis shows that the stars in the CoRoT fields present the same patterns found and reported on for the Galactic disk, showing a mixture of different populations associated with the Milky Way.

The stellar sample presents the same rotational behavior described in the literature for different evolutionary stages and colors. Also, we provide a calibration to derive $v \sin(i)$ from Hydra observations using the robust CCF technique (see Sect. 3.2 and Eq. (3)).

Finally, the present data set also represents an important piece of work to be used as standard sample calibration for different programs in the context of the CoRoT mission, since, among the brightest stars that comprise the CoRoT exoplanet field targets, dozens are included in the list of stars analyzed here. This work can also help to increase the scientific return of other spacial missions, such as *Gaia* or TESS.

Acknowledgements. Research activities of the Stellar Board of the Federal University of Rio Grande do Norte are supported by continuous grants of CNPq and FAPERN Brazilian agencies. We also acknowledges financial support of the INCT INEspaço. I.C.L. and C.E.F.L. acknowledges postdoctoral fellowship of the CNPq; C.C., S.C.M., C.E.F.L., S.V. and G.P.O. acknowledge graduate fellowships of the CAPES agency. This work was partially supported by the German Deutsche Forschungsgemeinschaft, DFG project number Ts 17/201. Support for C.C. and M.C. is provided by the Chilean Ministry for the Economy, Development, and Tourism's Programa Iniciativa Científica Milenio through grant IC 120009, awarded to the Millennium Institute of Astrophysics (MAS); by Proyecto Basal PFB- 06/2007; and by Proyecto FONDECYT Regular #1141141. This research has made use of the NASA/IPAC Extragalactic Database (NED) which is operated by the Jet Propulsion Laboratory, California Institute of Technology, under contract with the National Aeronautics and Space Administration.

References

Aigrain, S., Pont, F., Fressin, F., et al. 2009, A&A, 506, 425
Alonso, A., Arribas, S., & Martinez-Roger, C. 1996, A&A, 313, 873
Alonso, A., Arribas, S., & Martínez-Roger, C. 1999, A&AS, 140, 261
Alvarez, R., & Plez, B. 1998, A&A, 330, 1109
Asplund, M., Grevesse, N., & Sauval, A. J. 2005, in Cosmic Abundances as Records of Stellar Evolution and Nucleosynthesis, eds. T. G. Barnes III, & F. N. Bash, ASP Conf. Ser., 336, 25
Baglin, A., Auvergne, M., Barge, P., et al. 2007, in Fifty Years of Romanian Astrophysics, eds. C. Dumitrache, N. A. Popescu, M. D. Suran, & V. Mioc, AIP Conf. Ser., 895, 201
Ballester, P., Modigliani, A., Boitquin, O., et al. 2000, The Messenger, 101, 31
Barklem, P. S., & Aspelund-Johansson, J. 2005, A&A, 435, 373
Barklem, P. S., & Piskunov, N. 2003, in Modelling of Stellar Atmospheres, eds. N. Piskunov, W. W. Weiss, & D. F. Gray, IAU Symp., 210, 28
Barklem, P. S., Piskunov, N., & O'Mara, B. J. 2000a, A&AS, 142, 467
Barklem, P. S., Piskunov, N., & O'Mara, B. J. 2000b, A&A, 363, 1091
Bensby, T., Zenn, A. R., Oey, M. S., & Feltzing, S. 2007, ApJ, 663, L13
Boesgaard, A. M., & Tripicco, M. J. 1986, ApJ, 302, L49
Brown, J. A., Sneden, C., Lambert, D. L., & Dutchover, Jr., E. 1989, ApJS, 71, 293
Canto Martins, B. L., Lèbre, A., Palacios, A., et al. 2011, A&A, 527, A94
Carney, B. W., Latham, D. W., Stefanik, R. P., Laird, J. B., & Morse, J. A. 2003, AJ, 125, 293
Carney, B. W., Gray, D. F., Yong, D., et al. 2008, AJ, 135, 892
Cortés, C., Silva, J. R. P., Recio-Blanco, A., et al. 2009, ApJ, 704, 750
Cutispoto, G., Pastori, L., Pasquini, L., et al. 2002, A&A, 384, 491
De Medeiros, J. R., & Mayor, M. 1990, in Cool Stars, Stellar Systems, and the Sun, ed. G. Wallerstein, ASP Conf. Ser., 9, 404
De Medeiros, J. R., Da Rocha, C., & Mayor, M. 1996, A&A, 314, 499
De Medeiros, J. R., Do Nascimento, Jr., J. D., & Mayor, M. 1997, A&A, 317, 701
De Medeiros, J. R., do Nascimento, Jr., J. D., Sankarankutty, S., Costa, J. M., & Maia, M. R. G. 2000, A&A, 363, 239
Deleuil, M., Meunier, J. C., Moutou, C., et al. 2009, AJ, 138, 649
Flower, P. J. 1996, ApJ, 469, 355
Friel, E. D., Jacobson, H. R., & Pilachowski, C. A. 2010, AJ, 139, 1942
Gazzano, J.-C., de Laverny, P., Deleuil, M., et al. 2010, A&A, 523, A91
Girardi, L., Bressan, A., Bertelli, G., & Chiosi, C. 2000, A&AS, 141, 371
Gustafsson, B., Edvardsson, B., Eriksson, K., et al. 2008, A&A, 486, 951
Hill, V., Plez, B., Cayrel, R., et al. 2002, A&A, 387, 560
Hinkle, K., Wallace, L., Valenti, J., & Harmer, D. 2000, Visible and Near Infrared Atlas of the Arcturus Spectrum 3727–9300 Å (San Francisco: ASP)
Iben, Jr., I. 1967a, ApJ, 147, 650
Iben, Jr., I. 1967b, ApJ, 147, 624
Lèbre, A., de Laverny, P., de Medeiros, J. R., Charbonnel, C., & da Silva, L. 1999, A&A, 345, 936
Lucatello, S., & Gratton, R. G. 2003, A&A, 406, 691
Luck, R. E. 1977, ApJ, 218, 752
Luck, R. E., Andrievsky, S. M., Kovtyukh, V. V., Gieren, W., & Graczyk, D. 2011, AJ, 142, 51
Martell, S. L., & Shetrone, M. D. 2013, MNRAS, 430, 611
Meléndez, J., Asplund, M., Alves-Brito, A., et al. 2008, A&A, 484, L21
Meléndez, J., Ramírez, I., Casagrande, L., et al. 2010, Ap&SS, 328, 193
Melo, C. H. F., Pasquini, L., & De Medeiros, J. R. 2001, A&A, 375, 851
Nordström, B., Mayor, M., Andersen, J., et al. 2004, A&A, 418, 989
Pedicelli, S., Bono, G., Lemasle, B., et al. 2009, A&A, 504, 81
Pilachowski, C. A., Sneden, C., Kraft, R. P., Harmer, D., & Willmarth, D. 2000, AJ, 119, 2895
Plez, B. 1998, A&A, 337, 495
Recio-Blanco, A., Piotto, G., Aparicio, A., & Renzini, A. 2002, ApJ, 572, L71
Reddy, B. E., Lambert, D. L., & Allende Prieto, C. 2006, MNRAS, 367, 1329
Schlafly, E. F., & Finkbeiner, D. P. 2011, ApJ, 737, 103
Schlegel, D. J., Finkbeiner, D. P., & Davis, M. 1998, ApJ, 500, 525
Sebastian, D., Guenther, E. W., Schaffenroth, V., et al. 2012, A&A, 541, A34
Skrutskie, M. F., Meyer, M. R., Whalen, D., & Hamilton, C. 1996, AJ, 112, 2168
Soderblom, D. R. 1983, ApJS, 53, 1
Soderblom, D. R., Jones, B. F., Balachandran, S., et al. 1993, AJ, 106, 1059
Stetson, P. B., & Pancino, E. 2008, PASP, 120, 1332
Tonry, J., & Davis, M. 1979, AJ, 84, 1511
Torres, G. 2010, AJ, 140, 1158
van Dokkum, P. G. 2001, PASP, 113, 1420
Wallerstein, G., & Sneden, C. 1982, ApJ, 255, 577
Wallerstein, G., Bohm-Vitense, E., Vanture, A. D., & Gonzalez, G. 1994, AJ, 107, 2211